

## Article

# Role of Volatiles in the Evolution of a Carbonatitic Melt in Peridotitic Mantle: Experimental Constraints at 6.3 GPa and 1200–1450 °C

Aleksei Kruk and Alexander Sokol \*

V.S. Sobolev Institute of Geology and Mineralogy, Siberian Branch of the Russian Academy of Sciences, ave. Koptiyuga 3, 630090 Novosibirsk, Russia; krukana@igm.nsc.ru

\* Correspondence: sokola@igm.nsc.ru

**Abstract:** Reconstruction of the mechanisms of carbonatitic melt evolution is extremely important for understanding metasomatic processes at the base of the continental lithospheric mantle (CLM). We have studied the interaction between garnet lherzolite and a carbonatitic melt rich in molecular CO<sub>2</sub> and H<sub>2</sub>O in experiments at 6.3 GPa and 1200–1450 °C. The interaction with garnet lherzolite and H<sub>2</sub>O-bearing carbonatite melt leads to wehrlitization of lherzolite, without its carbonation. Introduction of molecular CO<sub>2</sub> and H<sub>2</sub>O initiates carbonation of olivine and clinopyroxene with the formation of orthopyroxene and magnesite. Partial carbonation leads to the formation of carbonate–silicate melts that are multiphase saturated with garnet harzburgite. Upon complete carbonation of olivine already at 1200 °C, melts with 27–31 wt% SiO<sub>2</sub> and MgO/CaO ≈ 1 are formed. At 1350–1450 °C, the interaction leads to an increase in the melt fraction and the MgO/CaO ratio to 2–4 and a decrease in the SiO<sub>2</sub> concentration. Thus, at conditions of a thermally undisturbed CLM base, molecular CO<sub>2</sub> and H<sub>2</sub>O dissolved in metasomatic agents, due to local carbonation of peridotite, can provide the evolution of agent composition from carbonatitic to hydrous silicic, i.e., similar to the trends reconstructed for diamond-forming high density fluids (HDFs) and genetically related proto-kimberlite melts.

**Keywords:** mantle; experiment; kimberlite; metasomatism; carbonatite; melt; fluid



**Citation:** Kruk, A.; Sokol, A. Role of Volatiles in the Evolution of a Carbonatitic Melt in Peridotitic Mantle: Experimental Constraints at 6.3 GPa and 1200–1450 °C. *Minerals* **2022**, *12*, 466. <https://doi.org/10.3390/min12040466>

Academic Editor: Jan C.M. De Hoog

Received: 24 February 2022

Accepted: 8 April 2022

Published: 11 April 2022

**Publisher's Note:** MDPI stays neutral with regard to jurisdictional claims in published maps and institutional affiliations.



**Copyright:** © 2022 by the authors. Licensee MDPI, Basel, Switzerland. This article is an open access article distributed under the terms and conditions of the Creative Commons Attribution (CC BY) license (<https://creativecommons.org/licenses/by/4.0/>).

## 1. Introduction

Reconstruction of the mechanism of kimberlite-like melt/fluid evolution in the continental lithospheric mantle (CLM) is an important issue of mantle petrology. There is extensive evidence that metasomatism of peridotite by carbonatite melts at the CLM base was a necessary preliminary step in kimberlite generation [1–6]. Micro-inclusions in fibrous diamonds are the most important source of information on the composition of metasomatic agents of kimberlitic affinity [7,8]. They are usually represented by a continuous series from K-rich carbonatite or saline to hydrous silicate HDFs [7–14] with variations in X<sub>CO<sub>2</sub></sub> values [CO<sub>2</sub>/(CO<sub>2</sub> + H<sub>2</sub>O) molar ratio] varying from 0.84 to almost zero [7,10,12,13]. Variations in the HDF composition may be as follows: (1) evolution by fractionation of carbonates and by immiscible separation into saline- and silicic-HDFs [9,15]; (2) fluid-mixing processes [11]; or (3) evolution of subduction zone HDFs upon interaction with peridotite of a CLM source [14].

At present, experimental substantiation of the mechanism of compositional evolution in metasomatic agents, from K-rich carbonatite to hydrous silicate melts/fluids, is problematic. Experiments in the peridotite–CO<sub>2</sub> ± H<sub>2</sub>O system and the results constraining reactions between peridotite and a carbonatitic melt support the stability of an alkali-rich SiO<sub>2</sub>-poor carbonatitic melt in peridotite of a thermally undisturbed CLM at 1200–1400 °C [16–21]. However, a “dry” carbonatitic melt equilibrated with peridotite can no longer evolve [19,21]. An H<sub>2</sub>O-bearing alkali-rich carbonatitic melt reacts with CLM peridotites to form carbonate–silicate melts with <20 wt% SiO<sub>2</sub> [16,17,19,21–23]. In this

case, the compositional evolution of the melt may proceed smoothly if the melt enters the lithospheric mantle through channels whose walls are changed due to carbonation freezing [21,24].

To date, there are two relatively poorly studied volatile components that may play an important role in the compositional evolution of carbonatitic melts and HDFs under CLM conditions. The first of them is chlorine [15,25]. Safonov et al. [15] showed that melting in the peridotite–carbonate–chloride system with 4.4 wt% Cl at 5.5 GPa provides a consistent change in the melt composition from essentially carbonatitic, with 2 wt% Cl, to carbonate–silicate (12–15 wt% SiO<sub>2</sub> and up to 14 wt% Cl) at 1360–1400 °C, and further to kimberlite-like (26–29 wt% SiO<sub>2</sub> and 4–6 wt% Cl) at 1500–1600 °C. In these systems at pressures of 7–16.5 GPa and in the presence of water, alkali-rich chloride–carbonate brine-like liquids can form above solidus [25]. Furthermore, at 1400–1600 °C, two immiscible carbonatite and chloride–carbonate liquids may coexist. The other component is molecular CO<sub>2</sub>. Very little is known about its solubility in carbonatitic melts at mantle P–T parameters. According to our estimates, the solubility of molecular CO<sub>2</sub> in a melt at 5.5 GPa and 1200–1450 °C decreases from 20–25 wt% at 4.5–6.8 wt% SiO<sub>2</sub> typical of carbonatite to below 7–12 wt% in more silicic melts with 26–32 wt% SiO<sub>2</sub> [22]. The influence of molecular CO<sub>2</sub> on the compositional evolution of the melt in the peridotite–carbonatite system at P–T parameters of the CLM base is almost unstudied, despite the fact that a CO<sub>2</sub> fluid occurs among inclusions in diamonds [26–28]. These studies are important because reconstruction of the mechanism of HDF composition transformation, from carbonatite to hydrous–silicic, may shed light on the genesis of kimberlite magmas and diamond.

Melts with an excess of CO<sub>2</sub> can originate in the hottest subduction zones (i.e., in ancient subduction zones or in sedimentary diapirs that have risen in the mantle wedge) during simultaneous melting of carbonated pelite [29–34] and partial decarbonation. The pelite decarbonation processes are confirmed by both calculations [35–37] and experimental studies [38,39]. In particular, at hottest subduction conditions, there may be decarbonation of Fe- and Fe–Mg–Ca carbonates with involvement of coesite and corundum/kyanite, which leads to the formation of pyrope–almandine–grossular garnet and CO<sub>2</sub> fluid. Notably, the siderite component is always present in the carbonate solid solution [33,39–42]. The presence of water should decrease the temperature at which the decarbonation reactions start [37]. A significant effect of the decarbonation reactions on the efficiency of carbonate transport into the mantle is evidenced by the fact that subduction of carbonate-rich sediments provides maximum volumetric emissions of isotopically heavy CO<sub>2</sub> through arc volcanic systems [43].

Experiments at 6.3 GPa and 1200–1450 °C reported in this paper aim at gaining insights into the role of molecular CO<sub>2</sub> in the transformation of a volatile-rich carbonatitic melt into a kimberlite-like melt (or carbonatite to hydrous silicate HDF growth media of fibrous diamonds) at its interaction with garnet lherzolite. The bulk composition of experimental systems was chosen to produce melt compositions similar to group I kimberlite by complete assimilation of garnet lherzolite in a carbonatitic melt. The P–T parameters of experiments reproduced a thermal regime of 38–45 mWt/m<sup>2</sup> in the subcratonic lithosphere at a depth of about 200 km.

## 2. Materials and Methods

### 2.1. Starting Compositions

The metasomatic agents were simulated by near-solidus melts produced by melting of carbonated pelite [32] and carbonated peridotite [44]. One composition was a K-rich melt (GS) which can form at 8 GPa and 1100 °C by melting of carbonated pelite (DG2) in subduction zones [32]. The other composition (B10) was a first-approximation model of an asthenospheric carbonatite melt that forms at 10 GPa and 1400 °C by melting of K-rich carbonated harzburgite [44]. Their phase composition at the experimental conditions was characterized by Sokol et al. [18]. Given the generally agreed assumption of high volatile contents in HDFs [7,10,12,13], we added molecular CO<sub>2</sub> and/or distilled H<sub>2</sub>O to the melts.

Peridotite from a CLM source of kimberlite was simulated by fresh garnet lherzolite from xenolith UD-05-05 of the Udachnaya-East kimberlite, Yakutia [45]. Garnet lherzolite used in our experiments contained slightly more FeO and less Al<sub>2</sub>O<sub>3</sub> (Table 1) than peridotite KLB-1 and HZ86 widely used in experimental petrology as a model mantle composition [46,47].

**Table 1.** Compositions of lherzolites from xenolith UD-05-05 (Lc), synthetic composition HZ86 (Lc), model carbonatitic melts (GS, B10) and bulk compositions of experimental samples.

	Lc (Ud-05-05)	Lc (HZ86)	B10	GS	Lc-B10	Lc-GS	Lc (HZ86)-B10 *	Lc (HZ86)-GS *
SiO <sub>2</sub>	43.24	45.75	16.01	0.62	34.25	29.18	32.17	29.5
TiO <sub>2</sub>	0.13	0.18	0.19	0.02	0.15	0.09	0.18	0.12
Al <sub>2</sub> O <sub>3</sub>	2.25	4.06	0.3	0.73	1.61	1.75	2.71	2.86
Cr <sub>2</sub> O <sub>3</sub>	0.68	0.47	0.11	0	0.49	0.46	0.34	0.3
FeO	11.19	7.53	18.31	3.97	13.54	8.81	11.41	6.25
MnO	0.11	0.11	0.34	0	0.19	0.07	0.19	0.07
NiO	0.25	0.35	0.08	0	0.19	0.17	0.25	0.22
MgO	39.02	37.73	22.21	4.77	33.47	27.72	32.14	25.86
CaO	2.72	3.21	8.3	15.67	4.56	6.99	5.04	7.7
Na <sub>2</sub> O	0.23	0.33	0.47	0.18	0.31	0.21	0.38	0.28
K <sub>2</sub> O	0.19	-	5.8	31.3	2.04	10.46	2.09	11.27
CO <sub>2</sub>	-	-	27.88	42.74	9.2	14.1	13.1	15.57
Total	100.01	99.69	100	100	100	100.01	100	100

\* compositions of the systems used in [18].

The model carbonatite compositions (Table 1) were produced by mixing pure carbonates (MgCO<sub>3</sub>, CaCO<sub>3</sub>, Na<sub>2</sub>CO<sub>3</sub>, and K<sub>2</sub>CO<sub>3</sub>) and oxides (MgO, SiO<sub>2</sub>, Al<sub>2</sub>O<sub>3</sub>, TiO<sub>2</sub>, FeO, etc.) in appropriate proportions. H<sub>2</sub>O and molecular CO<sub>2</sub> were added to the experimental mixtures as distilled water or oxalic acid (H<sub>2</sub>C<sub>2</sub>O<sub>4</sub>). At the applied pressure and temperature, anhydrous oxalic acid decomposed  $2\text{H}_2\text{C}_2\text{O}_4 \rightarrow 3\text{CO}_2 + 2\text{H}_2\text{O} + \text{C}^0$  providing CO<sub>2</sub> and H<sub>2</sub>O (3:2 mol) and C<sup>0</sup>. The composition of a fluid formed by oxalic acid decomposition was tested experimentally at 5.7 GPa and 1200–1420 °C [48]. Note that the content of H<sub>2</sub>O was close in water-containing and oxalic acid-containing samples. Thus, the effect of added CO<sub>2</sub> on melt evolution could be controlled.

Samples were placed in Au capsules for runs at 1200 °C or Pt capsules lined with 0.1 mm thick Re foil for higher-temperature runs at 1350 °C and 1450 °C. Au and Pt capsules were 2.0 mm and 5.0 mm in diameter, respectively, and had 0.2 mm-thick walls. The assembled capsules were sealed by Lampert PUK 4U high-frequency arc welding. The length/height of the assembled and press-molded capsules was 3.0 mm (Au) and 4.2 mm (Pt).

## 2.2. High Pressure Apparatus

Runs at 6.3 GPa were carried out in a split-sphere multi-anvil high-pressure apparatus [49]. The multi-anvil sphere of 8/6-type consisted of two anvils with square faces on the top and bottom and four side anvils with rectangular faces placed in an octahedral cavity formed by truncating the vertices of eight steel anvils. The sizes of high-pressure cells were 21.1 × 21.1 × 25.4 mm. Graphite heaters had a height of 18.5 mm and an inner diameter of 12.2 mm. Changes in the resistance of Bi at 2.55 GPa and PbSe at 4.0 and 6.8 GPa were used for calibration of pressure at room temperature. Bracketing the graphite-diamond equilibrium in the Ni<sub>0.7</sub>–Fe<sub>0.3</sub>–C system at 1350 °C was used for calibration of the cell at experimental conditions.

A PtRh<sub>6</sub>/PtRh<sub>30</sub> thermocouple was used for the measurement of temperature in each run. The thermocouple was calibrated at 6.3 GPa using the melting points of Al and Ag [50]. Pressures and temperatures were measured with an accuracy of ±0.1 GPa and ±20 °C, respectively [49,50]. The run duration varied from 40 to 150 h (Table 2). At the end of each experiment, samples were quenched at 150–200 deg/s under isobaric conditions.

**Table 2.** Experimental conditions and phase composition of samples.

Run ID	System	H <sub>2</sub> C <sub>2</sub> O <sub>4</sub> , wt%	H <sub>2</sub> O, wt%	Capsule Material	T, °C	t, h.	Phase Proportions, wt%					
							OI	Grt	Opx	Cpx	Mst	Liq
2200_2_1	Lc-B10	15.2	-	Au	1200	150	20	9	9	-	26	36
2200_2_2	Lc-B10	31.8	-	Au	1200	150	-	12	13	-	33	42
2200_2_3	Lc-GS	13.9	-	Au	1200	150	-	6	30	6	21	37
2200_2_4	Lc-GS	33.6	-	Au	1200	150	-	-	-	-	41	59
2215_2_3	Lc-B10	-	3	Au	1200	150	58	8	-	2	-	32
2200_2_6	Lc-GS	-	2.7	Au	1200	150	37	5	-	12	-	46
2200_2_7	Lc-B10	-	8	Au	1200	150	56	6	-	1	-	37
2200_2_8	Lc-GS	-	8.2	Au	1200	150	39	3	-	5	-	53
2190_2_1	Lc-B10	12.6	-	Pt + Re	1350	60	17	3	34	-	10	36
2190_2_2	Lc-GS	12.7	-	Pt + Re	1350	60	-	4	27	-	-	69
2190_2_3	Lc-B10	29.3	-	Pt + Re	1350	60	-	-	5	-	25	70
2211_2_1	Lc-GS	29.3	-	Pt + Re	1350	60	26	-	2	-	-	72
2192_2_1	Lc-B10	-	2.3	Pt + Re	1350	60	58	6	-	1	-	35
2192_2_2	Lc-GS	-	2.3	Pt + Re	1350	60	36	4	-	2	-	58
2192_2_3	Lc-B10	-	7.1	Pt + Re	1350	60	44	3	-	-	-	53
2192_2_4	Lc-GS	-	7.1	Pt + Re	1350	60	21	2	-	5	-	72
702_8_1	Lc-B10	12.7	-	Pt + Re	1450	40	3	10	36	-	-	51
702_8_2	Lc-GS	12.7	-	Pt + Re	1450	40	-	3	16	-	-	81
702_8_3	Lc-B10	-	3.2	Pt + Re	1450	40	44	5	-	-	-	51
702_8_4	Lc-GS	-	3	Pt + Re	1450	40	32	1	-	-	-	67

### 2.3. Analytical Techniques

After runs, recovered capsules were cleaned and dried. The capsules were sawed vertically in two halves. One half of each capsule was embedded in an epoxy resin by vacuum impregnation and then polished under kerosene, without the use of water. Samples were examined using a Tescan MIRA 3 LMU scanning electron microscope (SEM) and a Carl Zeiss Stemi 2000-C optical microscope (Jena, Germany). The solid phase compositions were studied using a MIRA 3 LMU scanning electron microscope (Tescan Orsay Holding, Brno, Czech Republic) coupled with an INCA energy-dispersive X-ray microanalysis system 450 equipped with a liquid nitrogen-free Large area EDS X-Max-80 Silicon Drift Detector (Oxford Instruments Nanoanalysis Ltd., High Wycombe, UK). The instruments were operated at an accelerating voltage of 20 kV, a beam current of 1 nA, and a spot diameter of ~10 µm for solid phases or ~100 µm for quenched melts. The live counting time for X-ray spectra was 20 s.

Electron microprobe analyses (EMPA) were performed at an accelerating voltage of 20 kV and a beam current of 30 nA using a Jeol JXA-8100 microanalyzer (Tokyo, Japan); the beam diameters were 1 to 2 µm for silicate and carbonate phases and 70–100 µm for quenched melts. Samples were sputter-coated with 20 nm carbon. The following standards were used: pyrope (O-145) for Si, Al, and Fe; Cr-garnet (Ud-92); Mn-garnet (Mn-IGEM); diopside for Mg and Ca; albite for Na; orthoclase for K; ilmenite for Ti; and spinel for Ni. The analytical error was 2 rel.%.

The weight proportions of phases in main runs were estimated by least-squares mass-balance calculations for a restricted number of components in the system: SiO<sub>2</sub>, TiO<sub>2</sub>, Al<sub>2</sub>O<sub>3</sub>, MgO, and CaO. The calculation results were additionally checked against SEM data in complicated cases.

## 3. Results

### 3.1. Sample Textures

In samples, a quenched melt was represented by an aggregate of dendritic silicate and carbonate crystals. The aggregate was located in hotter zones near side walls of Au capsules, 2 mm in diameter (Figures 1a–d and 2a–d; Table 2), or in relatively hotter sample parts of larger isometric Pt capsules, 5 mm in diameter (Figures 1e–h and 2e–h; Table 2). The degree

of sample melting at 1200 °C was greater than or close to the starting content of carbonatite B10 or GS in the system (33 wt%). The melt content ranged from 32 wt% to 46 wt% for small and from 36 wt% to 61 wt% for large additions of oxalic acid or H<sub>2</sub>O (Figure 3, Table 2). As temperature was rose to 1350 °C and 1450 °C, the degree of sample melting increased from 36 wt% to 81 wt% (Figure 3), reaching a maximum in Lc-GS-CO<sub>2</sub>-H<sub>2</sub>O samples with high CO<sub>2</sub> and H<sub>2</sub>O contents. In general, the melt concentration in Lc-B10-CO<sub>2</sub>-H<sub>2</sub>O samples was much lower than in Lc-GS-CO<sub>2</sub>-H<sub>2</sub>O samples (Figure 3). In none of the samples were globules of ultrapotassic silicate glass observed in the aggregate of quenched carbonate and silicate phases. We previously observed these globules at 5.5 GPa and 1350 °C [22] in Ls-GS-CO<sub>2</sub>-H<sub>2</sub>O samples with high CO<sub>2</sub> and H<sub>2</sub>O contents. As the amounts of CO<sub>2</sub> and H<sub>2</sub>O in samples increased, the quenching aggregate became looser due to the presence of numerous irregularly shaped microcavities between dendritic crystals (Figures 1 and 2). No isometric bubble holes were present in the samples.

Solid phases were located in colder capsule parts. Crystals synthesized in experiments at 1200 °C did not form special textures and were less than 200 µm in size (Figures 1a–d and 2a–d). In some samples, the phases produced at 1350–1450 °C formed tightly intergrown, often lenticular, magnesite and orthopyroxene aggregates (Figure 1f). Other samples contained aggregates of coarse-grained (up to 1 mm) olivine and/or orthopyroxene (Figures 1e and 2f) as well as usually subhedral, finer (100–500 µm) clinopyroxene and garnet crystals.

### 3.2. Phase Composition

Addition of either water or CO<sub>2</sub> and H<sub>2</sub>O led to the formation of different solid phase assemblages in equilibrium with the melt (Figure 3, Tables 2 and 3). In the Lc-B10-H<sub>2</sub>O and Lc-GS-H<sub>2</sub>O systems, samples produced at 1200–1350 °C, as well as the melt, contained olivine, clinopyroxene, and garnet, but lacked orthopyroxene and magnesite (Table 2, Figure 3). The content of olivine is maximal (up to 60 wt%) in the Lc-B10-H<sub>2</sub>O system at 1200 °C and decreases to slightly more than 40 wt% at 1350–1450 °C. In the Lc-GS-H<sub>2</sub>O system, the olivine concentration ranges from 20 to 40 wt%. The content of clinopyroxene is higher in the Lc-GS-H<sub>2</sub>O system. In this case, its content is higher in the samples produced at 1200 °C than at 1350 °C. At 1350 °C and the maximum concentration of water, clinopyroxene disappears in the Lc-B10-H<sub>2</sub>O system, but is present in the Lc-GS-H<sub>2</sub>O system. The content of garnet varies from sample to sample without a trend, whereas its amount usually decreases as the degree of sample melting increases.

The addition of CO<sub>2</sub> and H<sub>2</sub>O as oxalic acid (3:2 molar ratio) to the Lc-B10 system leads to the formation of magnesite and orthopyroxene as well as ≤50 µm fine graphite flakes. In the Lc-B10-CO<sub>2</sub>-H<sub>2</sub>O system, magnesite is absent only in the sample produced at 1450 °C. In this case, small additions of oxalic acid are accompanied by a decrease in the olivine concentration, but olivine is not completely carbonated. At large additions of oxalic acid, olivine is completely carbonated and magnesite becomes the main solid phase. The amount of garnet decreases as the degree of melting in the system increases.

In the Lc-GS-CO<sub>2</sub>-H<sub>2</sub>O system, olivine is not stable and the main solid phases are orthopyroxene, magnesite, clinopyroxene, and garnet. Magnesite is not present in this system at 1350 °C and 1450 °C. Thus, the interaction between garnet lherzolite and hydrous carbonatites B10 and GS leads to the disappearance of orthopyroxene and the formation of the Ol + Cpx + Grt + L assemblage. In Lc-B10-H<sub>2</sub>O, clinopyroxene is absent in one of the samples at 1350 °C and in all samples at 1450 °C. That is, the presence of water in a carbonatitic agent leads to wehrlitization of peridotite, but it does not undergo carbonation in the entire studied temperature range. Only the addition of molecular CO<sub>2</sub> and water at the 3:2 molar ratio to the systems provides carbonation of peridotite. In this case, as the amounts of added molecular CO<sub>2</sub> and H<sub>2</sub>O are increased, the degree of carbonation also rises. The interaction of garnet lherzolite with CO<sub>2</sub>- and H<sub>2</sub>O-bearing carbonatites B10 and GS leads to the formation of Opx ± Ol + Mgs + Grt + L assemblages, often without olivine and with a variable amount of orthopyroxene. In this case, in Lc-B10-CO<sub>2</sub>-

H<sub>2</sub>O samples with low contents of molecular CO<sub>2</sub>, the melt is multiphase saturated with magnesite-bearing garnet harzburgite.

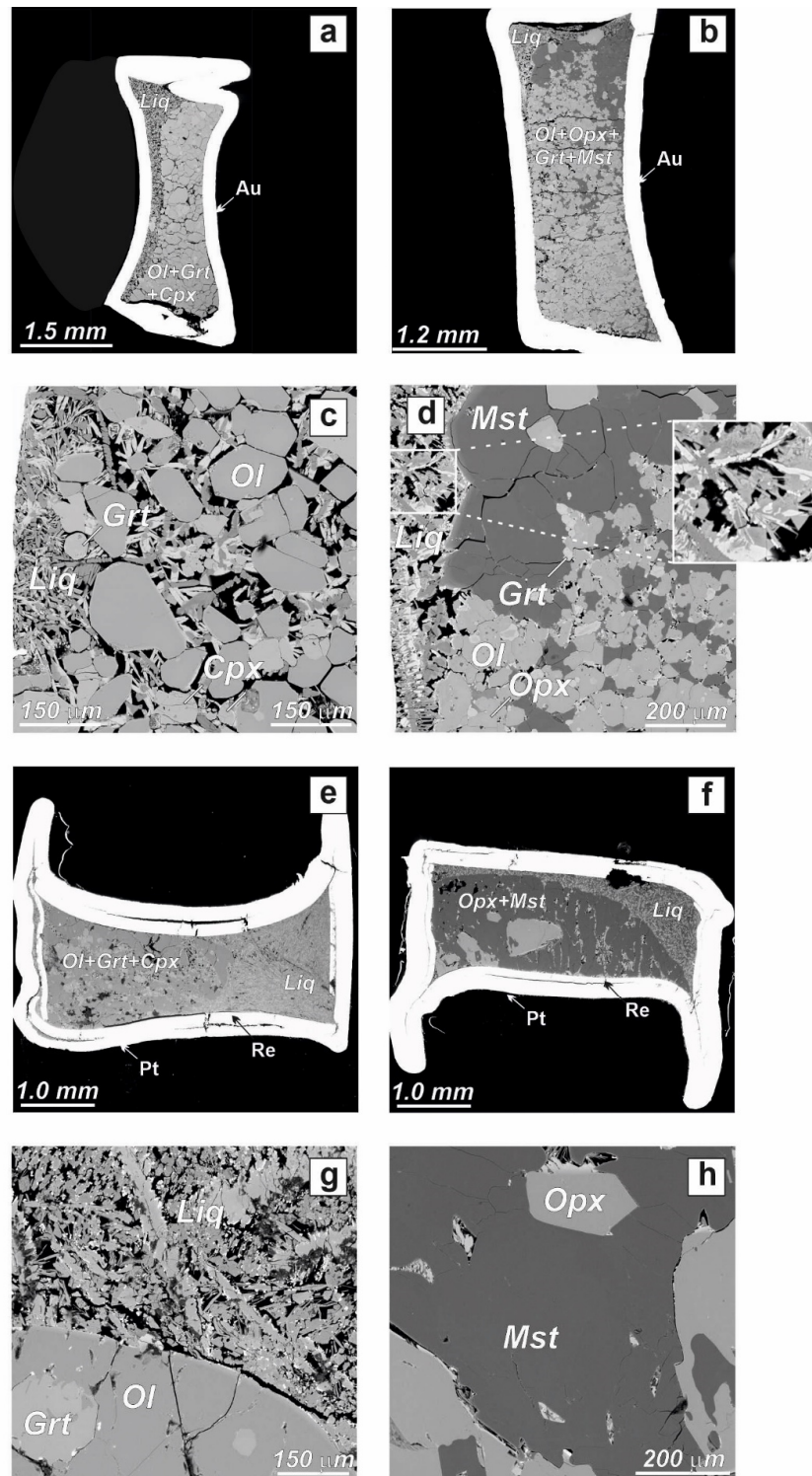


**Figure 1.** Backscatter electron images of representative run products in the lherzolite–carbonatite B10 (Lc-B10) system. (a,c): No. 2200\_2\_7 (T = 1200 °C; Lc-B10 with added H<sub>2</sub>O); (b,d): No. 2200\_2\_1 (T = 1200 °C; Lc-B10 with added CO<sub>2</sub> and H<sub>2</sub>O); (e,g): 2192\_2\_1 (T = 1350 °C; Lc-B10 with added H<sub>2</sub>O); (f,h): No. 2190\_2\_3 (T = 1350 °C; Lc-B10 with added CO<sub>2</sub> and H<sub>2</sub>O). Inset show microcavities between dendritic crystals. Abbreviations: Opx = orthopyroxene; Grt = garnet; Mgs = magnesite; Liq = melt.

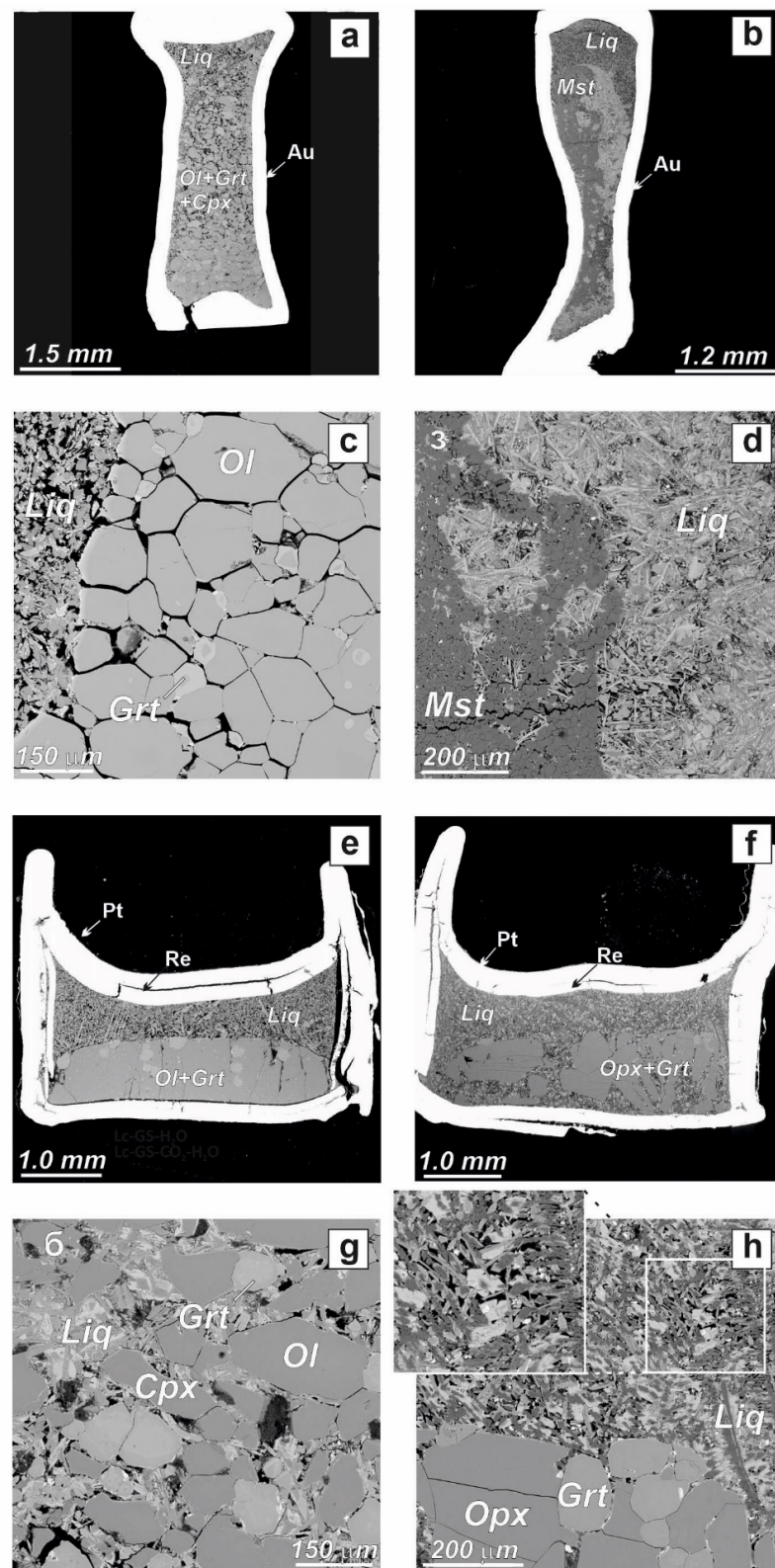


**Figure 2.** Backscatter electron images of representative run products in the lherzolite–carbonatite GS (Lc-GS) system. (a,c): No. 2200\_2\_6 (T = 1200 °C; Lc-GS with added H<sub>2</sub>O); (b,d): No. 2200\_2\_4 (T = 1200 °C; Lc-GS with added CO<sub>2</sub> and H<sub>2</sub>O); (e,g): 2192\_2\_4 (T = 1350 °C; Lc-GS with added H<sub>2</sub>O); (f,h): No. 2190\_2\_2 (T = 1350 °C; Lc-GS with added CO<sub>2</sub> and H<sub>2</sub>O). Insets show microcavities between dendritic crystals. Ol = olivine; Cpx = clinopyroxene; other abbreviations are as in Figure 1.

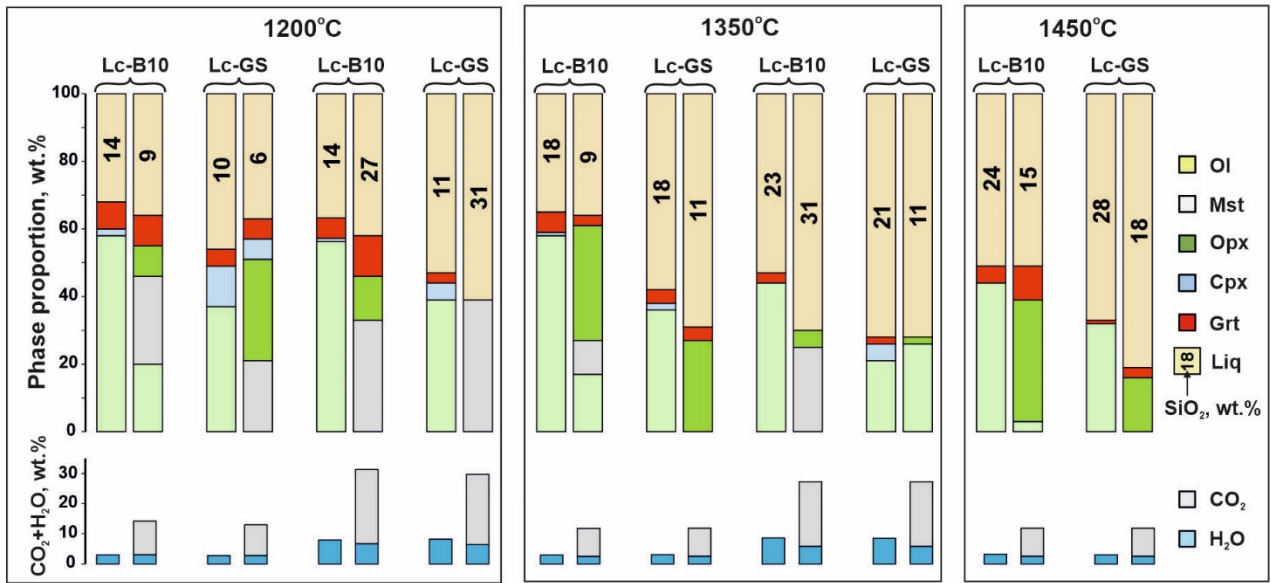


Figure 3. Phase relations in lherzolite-carbonatite B10 (Lc-B10) and lherzolite–GS (Lc-GS) samples as a function of temperature and amounts of added molecular CO<sub>2</sub> and H<sub>2</sub>O.

Table 3. Average compositions (wt%) of phases.

Run	Phase	SiO <sub>2</sub>	TiO <sub>2</sub>	Al <sub>2</sub> O <sub>3</sub>	Cr <sub>2</sub> O <sub>3</sub>	FeO	MnO	NiO	MgO	CaO	Na <sub>2</sub> O	K <sub>2</sub> O	Total
2200_2_1	Ol [8]	39.9 (2)	-	-	-	16.6 (3)	0.23 (6)	0.25 (6)	43.6 (3)	-	-	-	100.58
	Opx [7]	56.4 (3)	-	0.4 (1)	0.14 (3)	9.5 (10)	0.22 (4)	0.11 (2)	32.3 (7)	0.9 (2)	-	-	99.97
	Grt [5]	41.3 (1)	0.6 (2)	19.7 (1)	2.7 (3)	12 (2)	0.4 (1)	-	19 (1)	4.6 (4)	-	-	100.34
	Mst [6]	-	-	-	-	9.2 (6)	0.25 (2)	-	37.4 (4)	1.4 (2)	-	-	48.25
	Liq [8]	7 (2)	0.36 (9)	1.1 (4)	-	8.1 (8)	0.23 (4)	-	9 (3)	13 (4)	2.1 (7)	8 (2)	48.89
2200_2_2	Opx [5]	56.5 (4)	-	0.45 (5)	0.15 (4)	11 (1)	0.16 (1)	0.2 (3)	31.7 (9)	0.33 (4)	-	-	100.49
	Grt [4]	41.3 (3)	0.7 (3)	19.5 (3)	2.2 (4)	14 (3)	0.42 (8)	-	18 (2)	4.3 (2)	-	-	100.42
	Mst [7]	-	-	-	-	12 (3)	0.25 (6)	0.17 (2)	37 (2)	1 (3)	-	-	50.42
	Liq [7]	27 (4)	0.2 (1)	2.4 (10)	-	5 (1)	0.12 (3)	-	5 (1)	7 (2)	0.6 (2)	3 (1)	50.32
2200_2_3	Cpx [4]	55.5 (4)	-	0.7 (2)	0.28 (4)	4.1 (5)	-	-	18.9 (2)	20 (1)	0.32 (8)	0.19 (1)	100.06
	Opx [9]	57 (1)	-	0.7 (3)	0.3 (2)	7.8 (4)	0.12 (2)	0.11 (4)	33 (1)	1.4 (5)	0.15 (8)	0 (1)	100.58
	Grt [8]	42.2 (2)	0.3 (1)	20.4 (4)	2.1 (5)	11 (2)	0.3 (3)	-	19 (1)	5.2 (7)	-	-	100.5
	Mst [7]	-	-	-	-	6.69 (9)	0.11 (2)	-	38.2 (4)	1.36 (8)	-	-	46.36
	Liq [7]	6 (3)	0.2 (1)	0.7 (3)	-	5.7 (9)	0.11 (2)	-	10 (4)	9.6 (1)	0.9 (4)	19 (7)	52.21
2200_2_4	Mst [7]	0.1 (3)	-	-	-	9 (2)	0.14 (2)	0.14 (6)	37 (1)	1.8 (4)	-	-	48.18
2200_2_3	Liq [6]	31 (4)	0.14 (3)	2.9 (4)	0.23 (6)	4.4 (1)	-	-	7 (2)	11 (3)	0.1 (4)	9 (4)	65.77
2215_2_3	Ol [7]	40.7 (2)	-	-	-	11 (8)	-	-	48.3 (4)	-	-	-	100
	Cpx [5]	54.4 (3)	-	0.9 (1)	0.41 (7)	2.3 (1)	-	-	17.2 (3)	24.8 (5)	-	-	100.01
	Grt [5]	39.8 (3)	0.4 (1)	18 (1)	4.53 (8)	10.5 (9)	0.43 (1)	-	18.7 (7)	7.56 (3)	-	-	99.92
	Liq [7]	14 (1)	0.58 (3)	2.6 (2)	-	6 (1)	0.33 (4)	-	8 (5)	11 (2)	1.3 (4)	10 (4)	53.81
2200_2_6	Ol [7]	40.5 (1)	-	-	-	10.8 (4)	0.11 (2)	0.16 (6)	48.5 (4)	-	-	-	100.07
	Cpx [6]	55.3 (5)	-	0.54 (4)	0.18 (4)	3.2 (1)	-	-	19.1 (3)	21 (2)	0.2 (4)	0.22 (3)	99.74
	Grt [4]	42.2 (9)	0.5 (1)	20 (2)	3 (2)	9.4 (1)	0.34 (4)	-	19 (1)	5 (2)	-	-	99.44
	Liq [8]	10 (4)	0.18 (5)	1.2 (6)	-	6.1 (10)	0.12 (4)	-	12 (3)	8 (3)	0.8 (3)	19 (5)	57.4

Table 3. Cont.

Run	Phase	SiO <sub>2</sub>	TiO <sub>2</sub>	Al <sub>2</sub> O <sub>3</sub>	Cr <sub>2</sub> O <sub>3</sub>	FeO	MnO	NiO	MgO	CaO	Na <sub>2</sub> O	K <sub>2</sub> O	Total
2200_2_7	Ol [7]	40.5 (2)	-	-	-	14 (8)	0.18 (2)	0.22 (7)	44.9 (7)	-	-	-	99.8
	Cpx [5]	55.8 (3)	-	0.6 (5)	0.34 (5)	4.4 (2)	0.16 (1)	-	18.1 (5)	20.8 (1)	0.44 (7)	-	100.64
	Grt [7]	41.9 (4)	0.3 (2)	19.1 (8)	3.4 (5)	12 (1)	0.5 (1)	-	17 (2)	6 (1)	-	-	100.2
	Liq [8]	14 (3)	0.4 (1)	1.9 (3)	-	10 (1)	0.29 (7)	-	12 (2)	11 (2)	1.2 (6)	6 (2)	56.79
2200_2_8	Ol [8]	41.3 (2)	-	-	-	10.3 (6)	0.1 (2)	0.14 (6)	47.8 (5)	-	-	-	99.64
	Grt [9]	42.6 (3)	0.2 (1)	19.9 (4)	3.5 (4)	8.1 (4)	0.3 (2)	-	19 (1)	7 (2)	-	-	100.6
	Cpx [8]	55.9 (8)	-	0.56 (9)	0.25 (4)	2.7 (2)	-	-	18.4 (1)	21.7 (3)	0.18 (4)	0.3 (4)	99.99
	Liq [7]	12 (2)	0.14 (6)	2.4 (6)	-	5 (2)	0.13 (7)	-	10 (4)	10 (6)	0.7 (2)	13 (9)	53.37
2190_2_1	Ol [5]	39.9 (3)	-	-	-	12.7 (2)	0.15 (1)	0.37 (3)	47.4 (3)	-	-	-	100.52
	Opx [9]	57.4 (3)	-	0.54 (4)	0.15 (4)	7.4 (2)	0.15 (1)	0.11 (2)	34.1 (1)	0.38 (3)	-	-	100.27
	Grt [7]	42.2 (1)	0.2 (4)	19.6 (5)	2.9 (1)	11 (4)	0.37 (1)	-	21.3 (2)	2.2 (2)	-	-	99.77
	Mst [7]	-	-	-	-	6.8 (1)	0.19 (2)	0.1 (1)	38.2 (2)	0.91 (2)	-	-	46.2
	Liq [8]	9 (2)	0.36 (8)	0.8 (6)	-	11 (1)	0.34 (2)	-	21 (4)	12 (1)	0.4 (1)	2.4 (8)	57.3
2190_2_2	Opx [9]	58.4 (4)	-	0.6 (9)	0.2 (5)	3.5 (2)	-	-	36.9 (3)	0.44 (4)	-	-	100.04
	Grt [9]	43.2 (3)	0.12 (3)	20.7 (3)	2.6 (1)	5.8 (4)	0.21 (2)	-	24.3 (3)	2.8 (2)	-	-	99.73
	Liq [8]	11 (2)	0.13 (9)	1.4 (5)	-	4 (1)	0.14 (1)	-	19 (5)	10 (2)	0.36 (10)	11 (3)	57.03
2190_2_3	Opx [8]	57.9 (6)	-	0.39 (2)	0.21 (1)	7.5 (1)	0.13 (1)	0.18 (4)	33.9 (2)	0.17 (1)	-	-	100.38
	Mst [6]	-	-	-	-	7.1 (1)	0.15 (1)	0.16 (4)	38.5 (4)	0.43 (2)	-	-	46.34
	Liq [6]	31 (4)	0.13 (6)	1.6 (5)	0.14 (6)	8 (1)	0.2 (3)	-	18 (4)	4.5 (9)	0.23 (8)	0.7 (2)	64.5
2211_2_1	Ol [9]	41.6 (2)	-	-	-	8.2 (7)	0.1 (1)	0.18 (4)	50 (6)	-	-	-	100.08
	Opx [8]	56.1 (8)	-	0.67 (4)	0.31 (8)	2.6 (3)	-	-	18.9 (5)	21.1 (7)	0.2 (4)	0.3 (3)	100.18
	Liq [7]	11.2 (9)	0.19 (5)	1.4 (2)	-	4.3 (1)	0.14 (0)	-	10 (1)	9 (1)	0.38 (4)	19 (1)	55.61
2192_2_1	Ol [8]	39.9 (2)	-	-	-	13.8 (2)	0.22 (1)	0.25 (2)	46.2 (2)	-	-	-	100.37
	Cpx [6]	53.9 (4)	-	1 (6)	0.34 (4)	4.3 (2)	0.17 (1)	-	18.3 (3)	20.5 (3)	0.55 (5)	-	99.06
	Grt [6]	40.9 (7)	0.4 (2)	19 (1)	2 (1)	12 (2)	0.47 (7)	-	17 (2)	7 (2)	-	-	98.77
	Liq [9]	19 (3)	0.5 (1)	2 (3)	0.1 (3)	12 (2)	0.34 (4)	-	15 (2)	14 (4)	0.8 (3)	5.5 (9)	69.3
2192_2_2	Ol [7]	40.5 (4)	-	-	-	8.7 (6)	0.1 (1)	0.19 (3)	50.1 (5)	-	-	-	99.59
	Cpx [6]	54.3 (8)	-	1.1 (4)	0.4 (1)	3.7 (5)	0.12 (1)	-	20 (1)	18.3 (6)	0.5 (5)	0.17 (8)	98.59
	Grt [5]	41.8 (8)	0.3 (1)	20.1 (5)	2.8 (3)	7.8 (8)	0.29 (5)	-	21 (7)	5 (1)	-	-	99.09
	Liq [7]	18 (4)	0.2 (5)	1.8 (3)	-	7.7 (6)	0.17 (1)	-	18.2 (8)	12 (1)	0.61 (8)	11 (2)	69.68
2192_2_3	Ol [8]	39.6 (4)	-	-	-	11.15 (9)	0.18 (1)	0.25 (1)	48.4 (1)	-	-	-	99.58
	Grt [5]	41.7 (3)	0.11 (2)	18.5 (2)	3.8 (2)	9.8 (1)	0.46 (1)	-	20.3 (1)	5.1 (1)	-	-	99.77
	Liq [7]	23 (3)	0.25 (4)	2 (1)	0.19 (2)	11 (2)	0.33 (8)	-	17 (5)	9 (2)	0.3 (10)	2 (1)	65.07
2192_2_4	Ol [10]	40.9 (4)	-	-	-	6.7 (4)	-	0.16 (4)	52 (4)	-	-	-	99.76
	Cpx [6]	55.5 (1)	-	0.82 (5)	0.35 (5)	2.8 (1)	0.1 (1)	-	21.4 (6)	18.5 (8)	0.25 (6)	0.23 (4)	99.94
	Grt [9]	41.6 (6)	0.3 (2)	19.7 (6)	3.3 (7)	7 (1)	0.26 (5)	-	21.1 (6)	5.6 (8)	-	-	98.86
	Liq [7]	20.9 (8)	0.21 (2)	2 (2)	0.13 (1)	6.4 (4)	0.16 (1)	-	19 (1)	11.6 (7)	0.5 (1)	12.2 (5)	73.13
702_8_1	Ol [5]	42.8 (4)	-	0.19 (3)	-	10.9 (1)	0.14 (2)	0.39 (3)	46 (1)	0.17 (2)	-	-	100.76
	Grt [9]	43.4 (4)	-	20.6 (3)	2.7 (8)	7.3 (4)	0.28 (2)	-	24.7 (3)	1.09 (6)	-	-	100.07
	Opx [8]	57 (2)	-	0.9 (1)	0.2 (3)	5.4 (6)	0.14 (2)	-	35.5 (6)	0.3 (1)	-	-	99.44
	Liq [8]	15 (2)	0.27 (6)	1.8 (4)	0.12 (1)	9.7 (5)	0.36 (2)	-	29 (1)	8 (1)	0.47 (8)	3.2 (5)	67.92
702_8_2	Opx [9]	57.7 (5)	-	0.95 (5)	0.24 (4)	4 (8)	-	-	36.3 (3)	0.46 (2)	-	-	99.65
	Grt [7]	43.5 (3)	-	20.7 (2)	2.9 (3)	5.6 (4)	0.16 (1)	-	25.1 (4)	1.9 (3)	-	-	99.86
	Liq [8]	18 (5)	0.15 (1)	2 (5)	0.16 (4)	6.2 (3)	0.14 (1)	-	22 (2)	8 (1)	0.38 (8)	10 (2)	67.03
702_8_3	Ol [9]	40.7 (3)	-	-	-	10.92 (9)	0.18 (1)	0.26 (2)	47.8 (2)	-	-	-	99.86
	Grt [7]	42 (6)	0.13 (4)	18.6 (6)	3.5 (3)	9.5 (4)	0.38 (3)	-	20.3 (3)	5.2 (3)	-	0.3 (7)	99.91
	Liq [8]	24 (5)	0.3 (1)	3 (1)	0.21 (7)	13 (3)	0.37 (4)	-	22 (8)	9 (4)	0.7 (2)	4 (2)	76.58
702_8_4	Ol [7]	41.1 (4)	-	-	-	7.5 (9)	-	0.22 (1)	50.7 (2)	-	-	-	99.52
	Grt [9]	42.8 (8)	0.1 (3)	19.4 (3)	3.6 (1)	6.4 (3)	0.21 (1)	-	21.6 (5)	5.9 (5)	-	-	100.01
	Liq [8]	22 (2)	0.13 (3)	2.2 (2)	0.14 (2)	6.4 (6)	0.14 (1)	-	16 (2)	10.1 (9)	0.52 (8)	17 (3)	74.63

Number of analyses is shown in square brackets. Numbers in parentheses are one standard deviation in terms of the last significant digit.

### 3.3. Chemical Composition of Phases

#### 3.3.1. Melts in Water-Bearing Systems

The compositions of melts formed during the interaction of B10 and GS carbonatites with garnet lherzolite vary significantly, both with temperature and with the composition and amount of added volatiles. At the content of H<sub>2</sub>O from 3 wt% to 10 wt% in the Lc-B10-H<sub>2</sub>O system at temperature of 1200 °C, the SiO<sub>2</sub> content in melts is close to 14 wt% (Figure 4a,c). As temperature in the system rises to 1350–1450 °C, the SiO<sub>2</sub> content in the melt increases to 18–24 wt%. The SiO<sub>2</sub> concentration in melts produced in the Lc-GS-H<sub>2</sub>O system varies almost within the same limits as in the Lc-B10-H<sub>2</sub>O system, from 10–12 wt% at 1200 °C to 17–22 wt% at 1350–1450 °C. The variation range of Si + Al to Ca + Mg + Fe molar ratios, as it is not surprising, is minimal during the interaction between garnet lherzolite and hydrous carbonatite B10 (Figure 5). In this case, if the B10 composition is taken as the starting point, the produced melt compositions in the diagram Si + Al vs. Ca + Mg + Fe vs. K + Na (Figure 5a) are very close to the starting carbonatite. Melts produced in the Lc-GS-H<sub>2</sub>O system differ significantly more, relative to the starting GS composition; however, their final compositions are close to the compositions of melts from the Lc-B10-H<sub>2</sub>O system (Figure 5c).

#### 3.3.2. Melts in Systems with Addition of CO<sub>2</sub> and H<sub>2</sub>O

Addition of a molecular CO<sub>2</sub> and H<sub>2</sub>O mixture to the system led to a change in trends in melt composition variation. At small amounts of added CO<sub>2</sub> and H<sub>2</sub>O, variations in the SiO<sub>2</sub> and Al<sub>2</sub>O<sub>3</sub> concentrations as well as in the MgO/CaO ratio are small in comparison with water-bearing systems (Figure 4). For example, addition of 9–11 wt% CO<sub>2</sub> and 2.5–3 wt% H<sub>2</sub>O to the Lc-B10-CO<sub>2</sub>-H<sub>2</sub>O system leads to an increase in the SiO<sub>2</sub> concentration in the melt only up to 9 wt% at 1200–1350 °C and to 15 wt% at 1450 °C. The same amounts of CO<sub>2</sub> and H<sub>2</sub>O in the Lc-GS-CO<sub>2</sub>-H<sub>2</sub>O system lead to the formation of a melt with 6–11 wt% SiO<sub>2</sub> at 1200–1350 °C and 18 wt% SiO<sub>2</sub> at 1450 °C. At the same time, addition of 21–25 wt% CO<sub>2</sub> and 6–7 wt% H<sub>2</sub>O leads to a sharp increase in the SiO<sub>2</sub> concentration in melts already at 1200 °C up to 27 wt% in the Lc-B10-CO<sub>2</sub>-H<sub>2</sub>O system and up to 31 wt% in the Lc-GS-CO<sub>2</sub>-H<sub>2</sub>O system. As temperature is increased to 1350 °C, the content of SiO<sub>2</sub> in the melt remains at the same level in the Lc-B10-CO<sub>2</sub>-H<sub>2</sub>O system and drops to 11 wt% in the Lc-GS-CO<sub>2</sub>-H<sub>2</sub>O system. It is noted that the MgO/CaO ratios are close to 1 in all melts at 1200 °C and reach 3–4 in systems with addition of molecular CO<sub>2</sub> only at higher temperatures (Figure 4b,d). In this case, the Al<sub>2</sub>O<sub>3</sub> concentration increases and K<sub>2</sub>O decreases with an increase in the SiO<sub>2</sub> concentration in the melt. As temperature rises to 1450 °C, the melt composition almost does not change (Figure 4f).

#### 3.3.3. Solid Phases

The magnesium number of olivine in the Lc-GS system containing volatiles ranges from 89 at 1200 °C to 93 at 1350–1450 °C (Figure 6a). In the FeO-rich Lc-B10 system containing volatiles, it changes from 82 to 86 at 1200 °C and increases to 86–87 at 1350–1450 °C. Mg# of orthopyroxene changes from 84–89 at 1200 °C to 89–94 at 1350–1450 °C (Figure 6b). Ca# of clinopyroxene varies from 37 to 44. In produced garnets, the Cr<sub>2</sub>O<sub>3</sub> concentration weakly depends on the system composition and varies in a narrow range from 2.1 to 3.8 wt%, and the CaO concentration varies from 1.0 to 7.1 wt% (Figure 6c). The maximum CaO concentrations are observed in garnets from samples with water. Magnesites from relatively low temperature experiments contain FeO and CaO in a range of 7–12 wt% and 1.0–1.7 wt%, respectively. As temperature increases, their concentrations decrease to 7 wt% and <1 wt%, respectively.

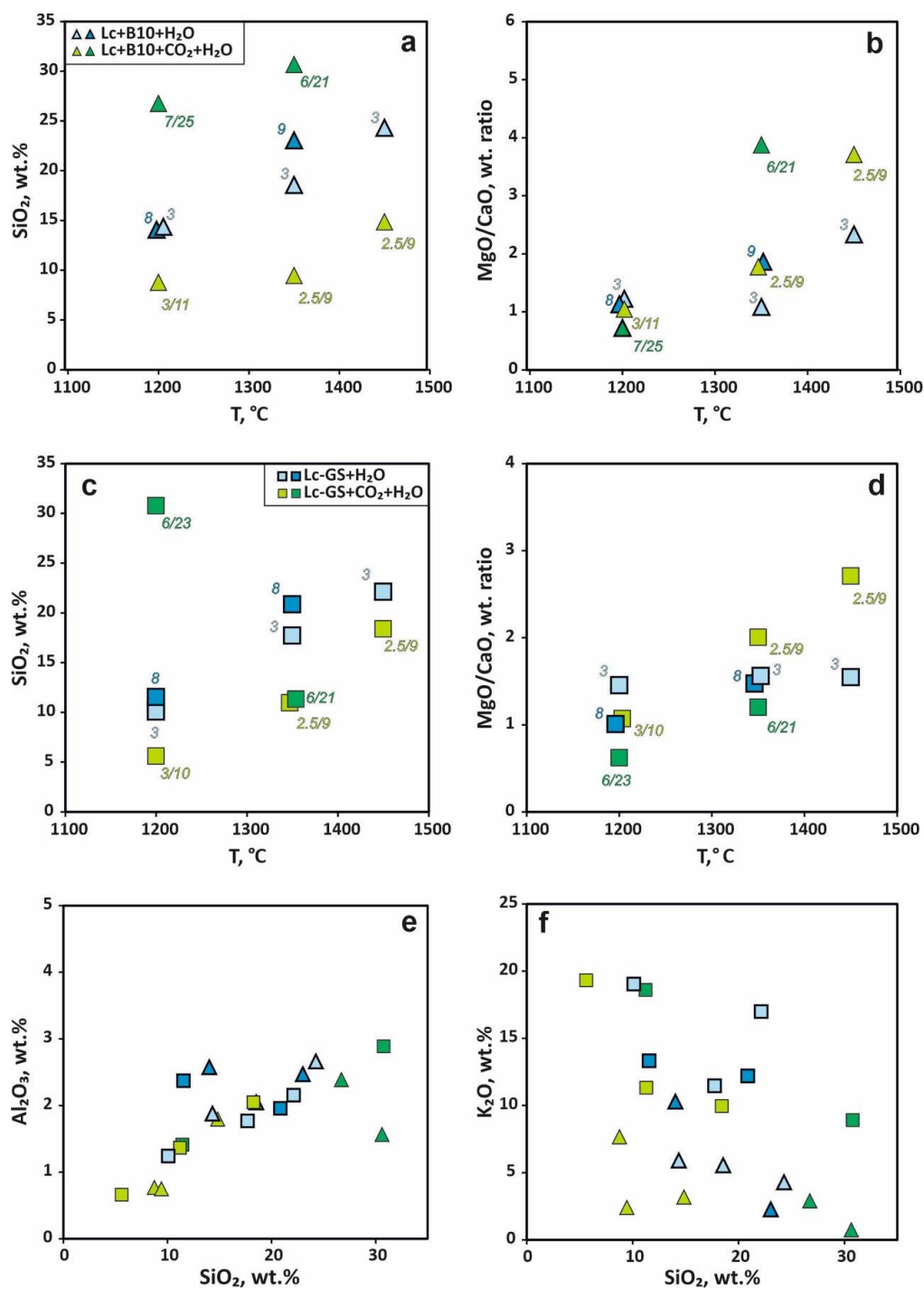


**Figure 4.** Major element compositions of experimental melts (on H<sub>2</sub>O-free basis). (a,b): temperature-dependent SiO<sub>2</sub> contents (a) and MgO/CaO weight ratio (b) in Lc-B10 samples; (c,d): temperature-dependent SiO<sub>2</sub> contents (c) and MgO/CaO weight ratio (d) in Lc-GS samples; (e): Al<sub>2</sub>O<sub>3</sub> vs. SiO<sub>2</sub> contents in Lc-B10 and Lc-GS samples; (f): K<sub>2</sub>O vs. SiO<sub>2</sub> contents in Lc-B10 and Lc-GS samples; Lc-B10-CO<sub>2</sub>-H<sub>2</sub>O = lherzolite–carbonatite B10 samples with added CO<sub>2</sub> and H<sub>2</sub>O; Lc-B10-H<sub>2</sub>O = lherzolite–carbonatite B10 samples with added H<sub>2</sub>O; Lc-GS-CO<sub>2</sub>-H<sub>2</sub>O = lherzolite–GS samples with added CO<sub>2</sub> and H<sub>2</sub>O (CO<sub>2</sub>/H<sub>2</sub>O content, wt%); Lc-GS-H<sub>2</sub>O = lherzolite–GS samples with added H<sub>2</sub>O (H<sub>2</sub>O content, wt%).

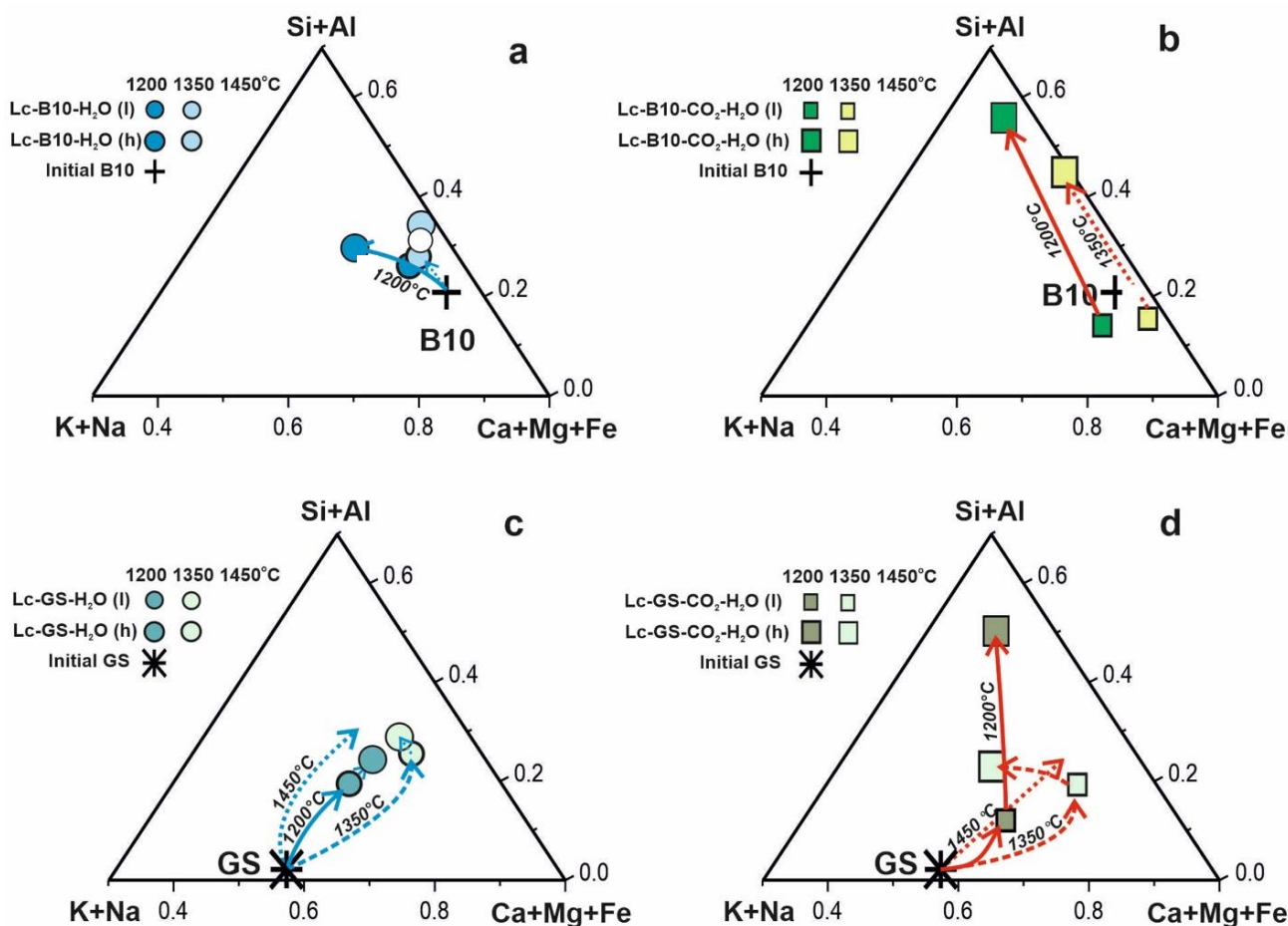


**Figure 5.** Ternary diagrams of Si + Al – Ca + Mg + Fe – Na + K (mol.%) for compositions of experimental melts and starting carbonatites B10 and GS. (a): Lc-B10-H<sub>2</sub>O system; (b): Lc-B10-CO<sub>2</sub>-H<sub>2</sub>O; (c): Lc-GS-H<sub>2</sub>O system; (d): Lc-GS-CO<sub>2</sub>-H<sub>2</sub>O system; l = low and h = high additive of molecular CO<sub>2</sub> and/or H<sub>2</sub>O.

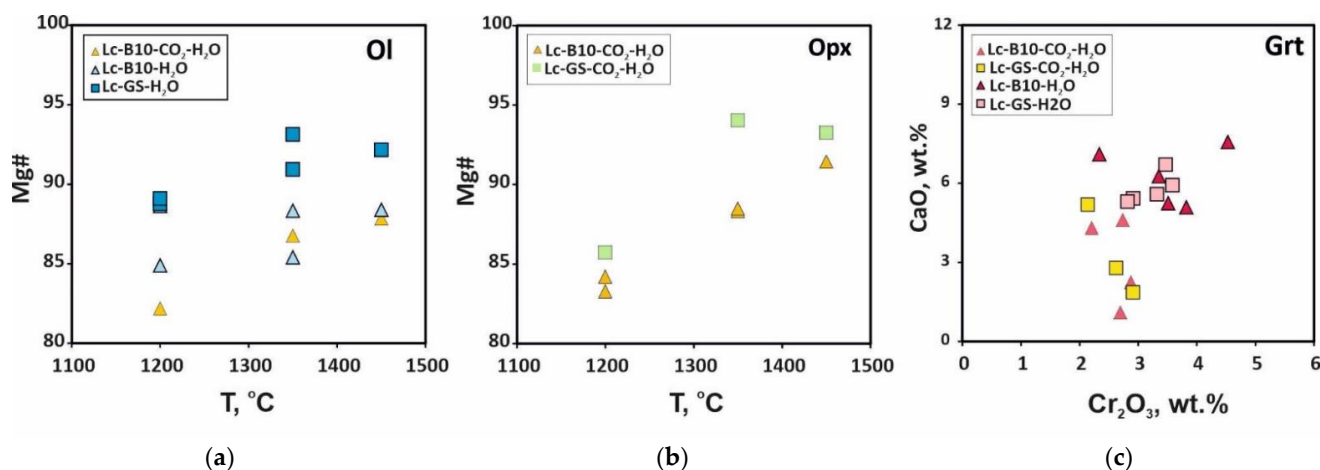


**Figure 6.** Compositions of olivine (a), orthopyroxene (b), and garnet (c) from samples produced by the interaction of lherzolite with volatile-rich carbonatitic melts.

#### 4. Discussion

##### 4.1. Carbonatite Melt-Peridotite Interaction

The data obtained in experiments at pressure of 6.3 GPa and temperature of 1200–1450 °C reveal main patterns of the interaction between garnet lherzolite and essentially carbonatitic

melts rich in molecular CO<sub>2</sub> and/or water, which may potentially be generated in different geodynamic settings. This interaction might occur during the metasomatism of peridotites of the CLM base and create prerequisites for the emergence of diamond-forming HDFs [8–14] and for the formation and separation of kimberlite magmas from a peridotite source [3–6,51].

To analyze how H<sub>2</sub>O and CO<sub>2</sub> additions to carbonatitic melts affect the phase relations in peridotite and the compositional evolution of the melt formed during the interaction, we used data on the same interaction, but with involvement of “dry” carbonatites B10 and GS, as a basis for comparison [18]. In the “dry” Lc-B10 system (Lc is HZ86, see Table 1) at 5.5–6.3 GPa and 1200 °C the melt–peridotite interaction occurred through Mg–Ca exchange, leading to elimination of orthopyroxene and crystallization of magnesite and clinopyroxene, resulting in the formation of the assemblage Ol + Cpx + Grt + Mgs + L (melt content is 14 wt%). At higher temperature of 1350 °C, the interaction in this system was accompanied by consumption of clinopyroxene and magnesite and by crystallization of orthopyroxene, resulting in the formation of the assemblage Ol + Opx + Cpx + Grt + L (L—20 wt%). At 6.3 GPa and 1350 °C, the assemblage Ol + Cpx + Grt + L (L—37 wt%) is present in the Lc-GS system. Typically, the SiO<sub>2</sub> content in all produced melts does not exceed 7 wt% [18]. Addition of water to Lc-B10 and Lc-GS (Lc is garnet lherzolite from xenolith UD-05-05) leads to the formation of the Ol + Cpx + Grt + L assemblage; in this case, the melt fraction in the Lc-B10-H<sub>2</sub>O system increases to 32–36 wt% at 1200 °C and 35–53 wt% at 1350 °C. An increase in temperature is accompanied by the disappearance of clinopyroxene in some samples. In the Lc-GS-H<sub>2</sub>O system, the degree of melting reaches 46–54 wt% at 1200 °C and 58–72 wt% at 1350 °C. In general, the emergence of water in the Lc-B10 and Lc-GS systems leads to a significant increase in the degree of reactive melting and the disappearance of magnesite even from low-temperature assemblages. Notably, the interaction of garnet lherzolite with hydrous carbonatites, as well as with “dry” ones, leads to wehrlitization of peridotite, but without its carbonation. As seen in the triangular diagrams (Figure 3), the melt composition significantly changes due to this interaction only in the Lc-GS-H<sub>2</sub>O system. In this case, the final compositions of equilibrium melts in the Lc-B10-H<sub>2</sub>O and Lc-GS-H<sub>2</sub>O systems are quite similar, differing only in the K<sub>2</sub>O concentration (Figure 3). Their content of SiO<sub>2</sub> varies from 10–14 wt% at 1200 °C to 18–28 wt% at 1350–1450 °C.

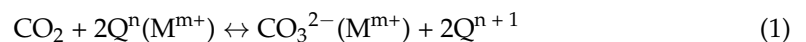
In the presence of molecular CO<sub>2</sub> and water in the Lc-B10 and Lc-GS systems, carbonation becomes the basis of the melt–peridotite interaction. For this reason, in the lherzolite matrix, the olivine and orthopyroxene ratios vary, and clinopyroxene disappears. Carbonate–silicate melts emerge; their compositions mainly depend on the concentration and composition of volatiles and temperature. The addition of 2–3 wt% H<sub>2</sub>O and 9–11 wt% molecular CO<sub>2</sub> to the Lc-B10-CO<sub>2</sub>-H<sub>2</sub>O system at 1200–1450 °C leads to the formation of carbonate–silicate melts that are multiphase saturated with the Ol–Opx–Grt ± Mgs assemblage (Figure 3). That is, the assemblage produced experimentally in the Lc-B10-CO<sub>2</sub>-H<sub>2</sub>O system reproduces mantle carbonated garnet harzburgite. In this system, magnesite is stable at 1200–1350 °C. At the same time, in the Lc-GS-CO<sub>2</sub>-H<sub>2</sub>O system, magnesite is stable only at 1200 °C, while olivine is not present, except for one sample at 1350 °C.

At first glance, the redox conditions in systems with addition of water alone and in systems with oxalic acid were noticeably different because elemental carbon was present among the decomposition products of oxalic acid. However, according to [48], the redox potential in cells used in our experiments is very close to EMOD. In the presence of carbonates/CO<sub>2</sub> in the systems, elemental carbon may spontaneously form due to influx of hydrogen into the Pt capsules from the cell materials. This suggests that, in long-term experiments, the oxygen fugacity in all capsules was similar and had no noticeable effect on phase equilibria.

In general, the melt–peridotite interaction in the “dry” systems occurred through Mg–Ca exchange, which ensured the replacement of clinopyroxene by orthopyroxene as temperature increased, with a high proportion of olivine being retained in the products [18]. In contrast, in systems with additions of molecular CO<sub>2</sub>, the interaction occurred through carbonation of olivine and, apparently, clinopyroxene. When the melt is the main calcium-

bearing phase, the role of Mg-Ca exchange between the solid phases and the melt for the melt–peridotite interaction becomes negligible

Sokol and Kruk [22] showed that carbonate–silicate melts equilibrated with carbonated harzburgite at 5.5 GPa and 1200–1450 °C may contain 4–8 wt% H<sub>2</sub>O, and the concentration of molecular CO<sub>2</sub> buffered by carbonation of olivine may vary from 15 wt% in kimberlite-like melts (at 1350–1450 °C) to 20 wt% in SiO<sub>2</sub>-poor, essentially carbonatitic melts (at 1200 °C). These estimates were made assuming that residual CO<sub>2</sub>, not consumed in the carbonation reaction, was dissolved in a carbonate–silicate melt as molecular CO<sub>2</sub>. This assumption is valid for SiO<sub>2</sub>-poor carbonatitic melts. However, silicate melts can dissolve CO<sub>2</sub> as CO<sub>3</sub><sup>2-</sup> ions [52,53] by the homogeneous reaction [54]:



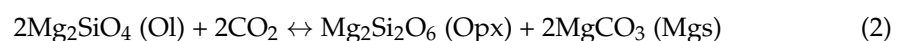
where Q<sup>n</sup> is a silica tetrahedron linked by bridging O atoms to n adjacent tetrahedra (zero n corresponds to an isolated SiO<sub>4</sub> tetrahedron); M<sup>m+</sup> denotes alkali or alkaline earth cations associated with non-bridging oxygen in Q<sup>n</sup> species and with oxygen in the CO<sub>3</sub><sup>2-</sup> complex. Data from [55] showed that the mole fraction of molecular CO<sub>2</sub> in the basaltic melt increases with temperature. In-situ infrared spectroscopy [56] studies of the speciation of carbon dioxide in diamond anvil cell experiments up to 1000 °C confirmed that the CO<sub>2</sub> + O<sup>2-</sup> = CO<sub>3</sub><sup>2-</sup> equilibrium in the melt shifted towards CO<sub>2</sub> with increasing temperature in dacite and phonolite melts. It is important to remember that in the presence of magnesite, the CO<sub>3</sub><sup>2-</sup> complex concentration in the melt cannot exceed some equilibrium value. Therefore, the contribution of the reaction in Equation (1) to the solubility of molecular CO<sub>2</sub> in the presence of magnesite-bearing assemblages is limited.

Redox reactions should occur concomitantly with local carbonation during the carbonatite melt–peridotite interaction. This is due to the fact that peridotites at depths of diamond formation in the CLM have oxygen fugacity below buffer enstatite–magnesite–olivine–diamond [57–59], and melts equilibrated with peridotite at the base of CLM cannot contain more than 10 wt% carbonates. Thus, oxidized volatile-rich carbonatitic melts can occur in the CLM only in a system of veins [6,24,60,61]. The redox interaction may lead to, on the one hand, local oxidation of the host peridotite [62] and, on the other hand, to the release of elemental carbon. It is noted that an alkali-rich carbonatite melt is known to be an effective growth environment for diamond [63–65].

#### 4.2. The Role of Volatiles in the Evolution of Melt Composition

The diagrams in Figure 4 show that the compositions of melts formed during these interactions evolve much more strongly in the Lc-B10-CO<sub>2</sub>-H<sub>2</sub>O and Lc-GS-CO<sub>2</sub>-H<sub>2</sub>O systems than in the Lc-B10-H<sub>2</sub>O and Lc-GS-H<sub>2</sub>O systems. This occurs only at a high concentration of molecular CO<sub>2</sub> and at relatively low temperature of 1200 °C. Under these conditions, the SiO<sub>2</sub> concentration in melts reaches 27–31 wt%, and the MgO/CaO ratio remains low, about 1. A similarly high concentration of SiO<sub>2</sub> in the melt is observed in the Lc-B10-CO<sub>2</sub>-H<sub>2</sub>O system at 1350 °C, with the MgO/CaO ratio being as high as 4 (Figure 4b). Comparison of these trends with the composition of solid phases in products (Figure 3) suggests that the SiO<sub>2</sub> content sharply increases if olivine is completely carbonated, and magnesite is present in equilibrium with the melt. The amount of added molecular CO<sub>2</sub> is also important for this mechanism as it ensures the binding of alkaline earth cations from the melt. For example, at 1200 °C and with a small amount of added CO<sub>2</sub> in the Lc-GS-CO<sub>2</sub>-H<sub>2</sub>O system, olivine partly disappears and magnesite is formed (Figures 2b,d and 3), but the melt remains essentially carbonatitic (Figure 4c).

The disappearance of olivine and an increase in orthopyroxene and magnesite suggest that additions of molecular CO<sub>2</sub> cause lherzolite carbonation mainly by the simplest reaction [66]:



The presence of clinopyroxene in samples with additions of H<sub>2</sub>O and its absence in samples with additions of molecular CO<sub>2</sub> + H<sub>2</sub>O suggest that clinopyroxene is also carbonated by the reaction [67]:



It is probable that carbonation of clinopyroxene concomitantly with carbonation of olivine provides a slight change in the MgO/CaO ratio in the melt at 1200 °C. In general, the revealed patterns in peridotite carbonation are close to those found at 1200–1350 °C and lower pressure of 5.5 GPa [22]. The reverse reaction of olivine and clinopyroxene carbonation in Equation (3) was proposed in [68] to substantiate the mechanism of transformation of carbonated melts to alkali basalts through their decarbonation and the release of CO<sub>2</sub>. According to [66], the direction of the reaction in Equation (3) may change from right to left at  $P < 3$  GPa. The obtained data suggest that a sharp increase in the SiO<sub>2</sub> concentration in the melt is possible only if activity of SiO<sub>2</sub> in the system is not buffered by a pair of olivine and orthopyroxene [69].

In order to show that the interactions in the Lc-B10 and Lc-GS systems with molecular CO<sub>2</sub> and H<sub>2</sub>O added give rise to unusual phase associations and a carbonate-silicate melt, we plotted histograms (Figure 7) comparing the phase relations determined experimentally and those calculated according to the model [21] at 6.3 GPa and 1200 °C. The bulk compositions of the experimental and calculated systems were identical. Obviously, the model [21] strongly overestimates orthopyroxene concentration compared to that in the experimental samples and, importantly, does not imply crystallization of magnesite in the systems. In addition, the model underestimates the melt contents and does not imply crystallization of garnet and clinopyroxene in the systems.

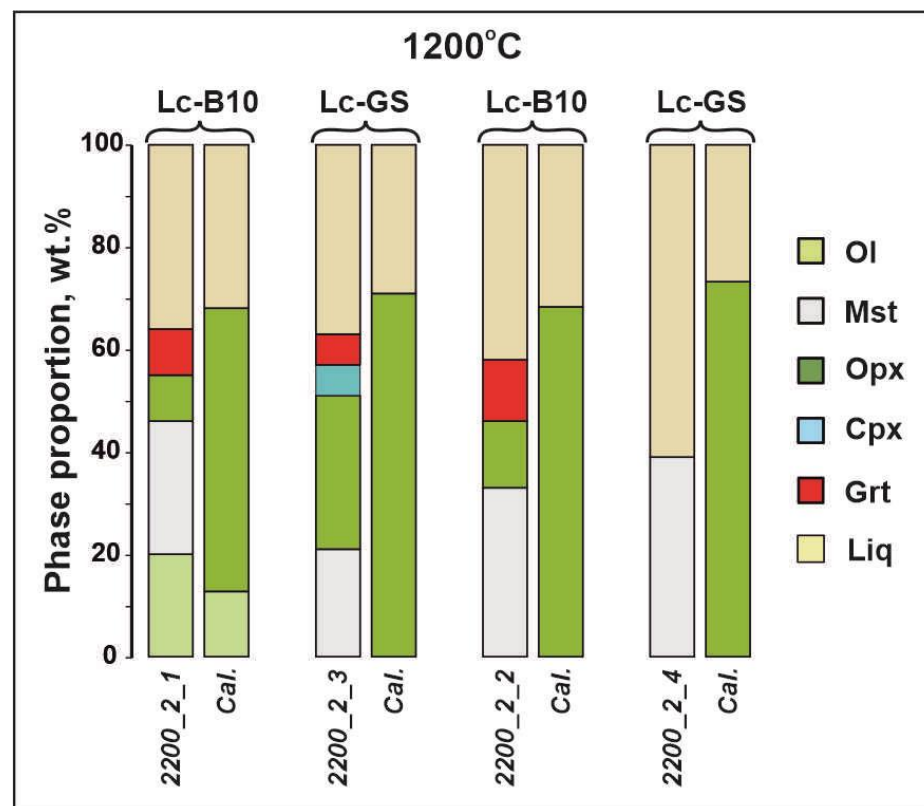


**Figure 7.** Plots showing the comparisons between phase proportions in the lherzolite-carbonatite B10 (Lc-B10) and lherzolite-GS (Lc-GS) systems with molecular CO<sub>2</sub> and H<sub>2</sub>O from the experiments conducted in this study at 6.3 GPa and 1200 °C (Exp.) and predicted phase proportions according to the model [21] under the same P-T conditions and at bulk compositions (Cal.).

Among the main volatile components of HDF fluids from inclusions in fibrous diamonds,  $\text{CO}_2$ ,  $\text{H}_2\text{O}$ , and Cl are traditionally considered. Their concentrations in inclusions can vary significantly [8–14]. Some inclusions contain a pure  $\text{CO}_2$  fluid or its mixture with  $\text{N}_2$  [26–28]. The reconstructed trends in melt composition variation are shown in Figure 8, together with the compositions of HDFs from fibrous diamonds across the world [11]. As seen, compositional variation in an ultrapotassic  $\text{CO}_2$ - and  $\text{H}_2\text{O}$ -bearing carbonatite GS melt (simulating melts from subduction zones) during its interaction with lherzolite (may be modeling the processes nearby subduct slabs where the carbonatite flux must be higher) under P-T conditions typical of the CLM (pressure of 6.3 GPa and temperature of 1200 °C) significantly reproduces the trend in HDF compositional variations, from essentially carbonatite to water-carbonate-silicate. The location of end points of the trend to the right of the shaded area of  $\text{SiO}_2$ -enriched HDF compositions is related, in our opinion, to the lack of chlorides in the experimental systems. The melt compositions in peridotite-carbonate-chloride systems do not evolve significantly as melting proceeds with an increase in temperature from 1200 °C to 1600 °C [15,25]. The composition of melts formed in these systems overlaps only a small part of the trend of HDFs from fibrous inclusions in diamonds and, moreover, at temperatures not typical of a thermal regime of the CLM base.

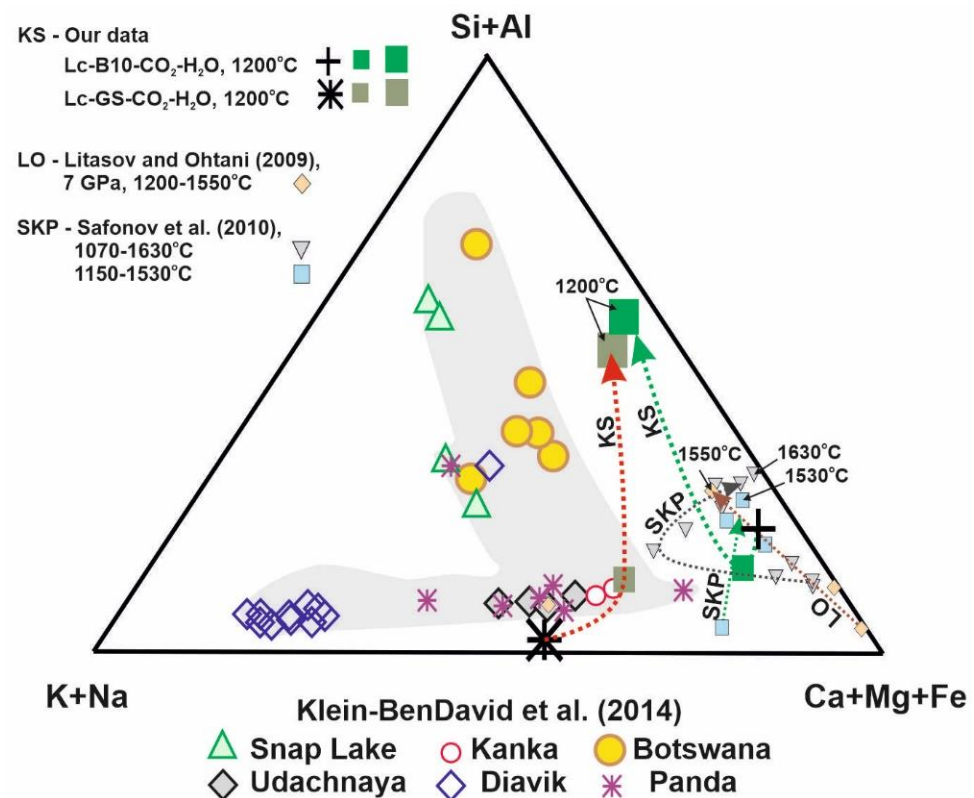


**Figure 8.** Ternary diagrams of Si + Al – Ca + Mg + Fe – Na + K (mol.%) for the average major element composition of micro-inclusions in diamonds [11] and trends in the evolution of experimentally produced melts in systems: peridotite–carbonate–chloride [15,25], Lc-B10- $\text{CO}_2$ - $\text{H}_2\text{O}$ , and Lc-GS- $\text{CO}_2$ - $\text{H}_2\text{O}$  (this study).

Therefore, the factors that might potentially enable the evolution of diamond-forming HDFs and genetically related proto-kimberlite melts during interaction with peridotites under the CLM base thermal regime include the influence of molecular  $\text{CO}_2$  and  $\text{H}_2\text{O}$  as well as the processes of liquid immiscibility [15,22,34,45,70]. The found patterns are applicable to cases where potential metasomatic agents in the mantle are represented by carbonatitic melts with excess  $\text{CO}_2$ . They can be generated during the melting of carbonated rocks, which is associated with their partial decarbonation at conditions of

hottest subduction (in ancient subduction zones or in sedimentary diapirs that have risen in the mantle wedge). It is the excess CO<sub>2</sub> that can enable the trends in the evolution of metasomatic agents, reconstructed from diamond inclusions. Furthermore, the evolution becomes possible during the interaction of agents with peridotite, as it was suggested in [14], and in a temperature range of 1200–1400 °C, which is fixed by thermobarometry for the deepest kimberlite xenoliths [71,72]. Regarding the genesis of kimberlite magmas, the contents of molecular CO<sub>2</sub> and H<sub>2</sub>O may largely control the composition of an evolving proto-kimberlite melt released from the source. In all cases, SiO<sub>2</sub>-rich melts/fluids formed during the evolution may only be locally stable, apparently in the veins system, equilibrated with strongly metasomatized peridotites. Our results have confirmed that the presence of water alone in carbonatitic melts cannot ensure its transformation into hydrous silicate HDFs by metasomatic reactions.

## 5. Conclusions

The reported experimental results at 6.3 GPa and 1200–1450 °C show that molecular CO<sub>2</sub> and water may play an important role in the compositional evolution of carbonatitic melts during their interaction with peridotites of the CLM base. The revealed trends in the compositional evolution of volatile-rich carbonatitic melts reproduce both some trends in HDF composition variations in fibrous diamonds and the transformation of carbonatitic melts into kimberlite-like ones at moderate temperatures of 1200–1350 °C and depths of about 200 km. The following most important factors in the evolution of a carbonatitic melt during its interaction with CLM peridotites may be formulated:

1. The metasomatic interaction with peridotite should occur in a limited volume, only near the walls of veins that form networks in the CLM. The walls of feeder channels are passivated from the interaction with an aggressive carbonatitic melt due to redox freezing.
2. Temperature of the interaction should not exceed 1200–1350 °C, which corresponds to an undisturbed thermal regime of the CLM base with a heat flux of about 40 mW/m<sup>2</sup>. Elevation of temperature above this interval leads to a sharp increase in the melting volume of peridotite and a decrease in the SiO<sub>2</sub> concentration of the resulting melt/fluid.
3. The concentration of water in the melt should not inhibit local carbonation of olivine during peridotite metasomatism.
4. The presence of dissolved molecular CO<sub>2</sub> (at a molar water to molecular CO<sub>2</sub> ratio of ~2:3) in a carbonatitic melt in amounts that enable complete carbonation of olivine in the contact zone, such that the orthopyroxene + magnesite assemblage or only magnesite should remain in the channel walls. Due to this, even at 1200 °C, the content of SiO<sub>2</sub> in the melt formed upon the interaction with peridotite may reach 27–31 wt%. If olivine remains stable at the reaction front, the SiO<sub>2</sub> concentration in the melt is less than 10–11 wt%.

**Author Contributions:** Conceptualization, A.K. and A.S.; methodology, A.S.; validation, A.K. and A.S.; formal analysis, A.K.; investigation, A.K. and A.S.; resources, A.K. and A.S.; data curation, A.K. and A.S.; writing—original draft preparation, A.K. and A.S.; writing—review and editing, A.K. and A.S.; visualization, A.K.; supervision, A.S.; project administration, A.K.; funding acquisition, A.K. All authors have read and agreed to the published version of the manuscript.

**Funding:** This research was funded by Russian Science Foundation, grant number 19-77-10023.

**Acknowledgments:** We are grateful to V.S. Shatskii and A.L. Ragozin for providing xenolith sample Ud-05-05 for our experiments. The SEM, EDS and EPMA studies of experimental samples were performed at the Analytical Center for Multi- elemental and Isotope Research (IGM SB RAS, Novosibirsk).

**Conflicts of Interest:** The authors declare no conflict of interest.

## References

1. Wyllie, P.J. Magmas and volatile components. *Am. Mineral.* **1979**, *64*, 469–500.
2. Wyllie, P.J. The origin of kimberlite. *J. Geophys. Res.* **1980**, *85*, 6902–6910. [[CrossRef](#)]
3. Boyd, F.R.; Pokhilenko, N.P.; Pearson, D.G.; Mertzman, S.A.; Sobolev, N.V.; Finger, L.W. Composition of the Siberian cratonic mantle: Evidence from Udachnaya peridotite xenoliths. *Contrib. Mineral. Petrol.* **1997**, *128*, 228–246. [[CrossRef](#)]
4. Becker, M.; Le Roex, A.P. Geochemistry of South African on- and off-craton, group I and group II kimberlites: Petrogenesis and source region evolution. *J. Petrol.* **2006**, *47*, 673–703. [[CrossRef](#)]
5. Pearson, D.G.; Wittig, N. The formation and evolution of cratonic mantle lithosphere—Evidence from mantle xenoliths. *Treatise Geochem.* **2014**, *3*, 255–292.
6. Doucet, L.S.; Peslier, A.H.; Ionov, D.A.; Brandon, A.D.; Golovin, A.V.; Ashchepkov, I.V. High water content in the Siberian cratonic mantle linked to melt metasomatism: An FTIR study of Udachnaya peridotite xenoliths. *Geochim. Cosmochim. Acta* **2014**, *137*, 159–187. [[CrossRef](#)]
7. Schrauder, M.; Navon, O. Hydrous and carbonatitic mantle fluids in fibrous diamonds from Jwaneng, Botswana. *Geochim. Cosmochim. Acta* **1994**, *58*, 761–771. [[CrossRef](#)]
8. Navon, O. Diamond formation in the Earth's mantle. In Proceedings of the VII International Kimberlite Conference 2. Red Roof Design, Cape Town, South Africa, 11–17 April 1998; pp. 584–604.
9. Klein-BenDavid, O.; Izraeli, E.S.; Hauri, E.; Navon, O. Fluid inclusions in diamonds from the Diavik mine, Canada and the evolution of diamond-forming fluids. *Geochim. Cosmochim. Acta* **2007**, *71*, 723–744. [[CrossRef](#)]
10. Klein-BenDavid, O.; Logvinova, A.; Schrauder, M.; Spetius, Z.; Weiss, Y.; Hauri, E.; Kaminsky, F.V.; Sobolev, N.V.; Navon, O. High-Mg carbonatitic microinclusions in some Yakutian Diamonds— a new type of diamond-forming fluid. *Lithos* **2009**, *112S*, 648–659. [[CrossRef](#)]
11. Klein-BenDavid, O.; Pearson, D.G.; Nowell, G.M.; Ottley, C.; McNeill, J.C.; Logvinova, A.; Sobolev, N.V. The sources and time-integrated evolution of diamond-forming fluids—Trace elements and isotopic evidence. *Geochim. Cosmochim. Acta* **2014**, *125*, 146–169. [[CrossRef](#)]
12. Zedgenizov, D.A.; Ragozin, A.L.; Shatsky, V.S.; Araujo, D.; Griffin, W.L.; Kagi, H. Mg and Fe-rich carbonate-silicate high-density fluids in cuboid diamonds from the Internationalnaya kimberlite pipe (Yakutia). *Lithos* **2009**, *112* (Suppl. 2), 638–647. [[CrossRef](#)]
13. Kopylova, M.; Navon, O.; Dubrovinsky, L.; Khachatryan, G. Carbonatitic mineralogy of natural diamond-forming fluids. *Earth Planet. Sci. Lett.* **2010**, *291*, 126–137. [[CrossRef](#)]
14. Weiss, Y.; McNeill, J.; Pearson, D.G.; Nowell, G.M.; Ottley, C.J. Highly saline fluids from a subducting slab as the source for fluid-rich diamonds. *Nature* **2015**, *524*, 339–342. [[CrossRef](#)] [[PubMed](#)]
15. Safonov, O.G.; Kamenetsky, V.S.; Perchuk, L.L. Links between carbonatite and kimberlite melts in chloride–carbonate–silicate systems: Experiments and application to natural assemblages. *J. Petrol.* **2011**, *52*, 1307–1331. [[CrossRef](#)]
16. Brey, G.P.; Bulatov, V.K.; Girmis, A.V. Influence of water and fluorine on melting of carbonated peridotite at 6 and 10 GPa. *Lithos* **2009**, *112*, 249–259. [[CrossRef](#)]
17. Girmis, A.V.; Bulatov, V.K.; Brey, G.P. Formation of primary kimberlite melts—Constraints from experiments at 6–12 GPa and variable CO<sub>2</sub>/H<sub>2</sub>O. *Lithos* **2011**, *127*, 401–413. [[CrossRef](#)]
18. Sokol, A.G.; Kruk, A.N.; Chebotarev, D.A.; Palyanov, Y.N. Carbonatite melt–peridotite interaction at 5.5–7.0 GPa: Implications for metasomatism in lithospheric mantle. *Lithos* **2016**, *248*, 66–79. [[CrossRef](#)]
19. Sokol, A.G.; Kruk, A.N.; Palyanov, Y.N.; Sobolev, N.V. Stability of phlogopite in ultrapotassic kimberlite-like systems at 5.5–7.5 GPa. *Contrib. Mineral. Petrol.* **2017**, *172*, 21. [[CrossRef](#)]
20. Kruk, A.N.; Sokol, A.G.; Palyanov, Y.N. Phase relations in the harzburgite–hydrous carbonate melt at 5.5–7.5 GPa and 1200–1350 °C. *Petrology* **2018**, *26*, 575–587. [[CrossRef](#)]
21. Sun, C.; Dasgupta, R. Slab–mantle interaction, carbon transport, and kimberlite generation in the deep upper mantle. *Earth Planet. Sci. Lett.* **2019**, *506*, 38–52. [[CrossRef](#)]
22. Sokol, A.G.; Kruk, A.N. Role of CO<sub>2</sub> in the evolution of Kimberlite Magma: Experimental constraints at 5.5 GPa and 1200–1450 °C. *Lithos* **2021**, *386*, 106042. [[CrossRef](#)]
23. Stamm, N.; Schmidt, M.W. Asthenospheric kimberlites: Volatile contents and bulk compositions at 7 GPa. *Earth Planet. Sci. Lett.* **2017**, *474*, 309–321. [[CrossRef](#)]
24. Foley, S.F. A reappraisal of redox melting in the Earth's mantle as a function of tectonic setting and time. *J. Petrol.* **2011**, *52*, 1363–1391. [[CrossRef](#)]
25. Litasov, K.D.; Ohtani, E. Phase relations in the peridotite–carbonate–chloride system at 7.0–16.5 GPa and the role of chlorides in the origin of kimberlite and diamond. *Chem. Geol.* **2009**, *262*, 29–41. [[CrossRef](#)]
26. Navon, O.; Hutcheon, I.D.; Rossman, G.R.; Wasserburg, G.J. Mantle-derived fluids in diamond micro-inclusions. *Nature* **1988**, *335*, 784–789. [[CrossRef](#)]
27. Tomilenko, A.A.; Ragozin, A.L.; Shatskii, V.S.; Shebanin, A.P. Variation in the fluid phase composition in the process of natural diamond crystallization. *Dokl. Earth Sci.* **2001**, *379*, 571–574.
28. Smith, E.M.; Kopylova, M.G.; Frezzotti, M.L.; Afanasiev, V.P. Fluid inclusions in Ebelyakh diamonds: Evidence of CO<sub>2</sub> liberation in eclogite and the effect of H<sub>2</sub>O on diamond habit. *Lithos* **2015**, *216*, 106–117. [[CrossRef](#)]

29. Tsuno, K.; Dasgupta, R. The effect of carbonates on near-solidus melting of pelite at 3 GPa: Relative efficiency of H<sub>2</sub>O and CO<sub>2</sub> subduction. *Earth Planet. Sci. Lett.* **2012**, *319*, 185–196. [[CrossRef](#)]
30. Tsuno, K.; Dasgupta, R.; Danielson, L.; Richter, K. Flux of carbonate melt from deeply subducted pelitic sediments: Geophysical and geochemical implications for the source of Central American volcanic arc. *Geophys. Res. Lett.* **2012**, *39*, L16307. [[CrossRef](#)]
31. Dasgupta, R. Ingassing, storage, and outgassing of terrestrial carbon through geologic time. *Rev. Min. Geochem.* **2013**, *75*, 183–229. [[CrossRef](#)]
32. Grassi, D.; Schmidt, M.W. Melting of carbonated pelites at 8–13 GPa: Generating K-rich carbonatites for mantle metasomatism. *Contrib. Mineral. Petrol.* **2011**, *162*, 169–191. [[CrossRef](#)]
33. Schmidt, M.W.; Poli, S. Devolatilization During Subduction. *Treatise Geochem.* **2014**, *4*, 669–701. [[CrossRef](#)]
34. Shatskiy, A.F.; Arefiev, A.V.; Podborodnikov, I.V.; Litasov, K.D. Origin of K-rich diamond-forming immiscible melts and CO<sub>2</sub> fluid via partial melting of carbonated pelites at a depth of 180–200 km. *Gondwana Res.* **2019**, *75*, 154–171. [[CrossRef](#)]
35. Berman, R.G. Thermobarometry using multiequilibrium calculations: A new technique with petrologic applications. *Can. Miner.* **1991**, *29*, 833–855.
36. Luth, R.W. Carbon and carbonates in mantle. In *Mantle Petrology: Field Observation and High Pressure Experimentation: A Tribute to Francis, R. (Joe) Boyd*; Fei, Y., Bertka, M.C., Mysen, B.O., Eds.; The Geochemical Society: Washington, DC, USA, 1999; pp. 297–316. ISBN 0-941809-05-6.
37. Ogasawara, Y.; Liou, J.G.; Zhang, R.Y. Thermochemical calculation of logfO<sub>2</sub>-T-P stability relations of diamond-bearing assemblages in the model system CaO-MgO-SiO<sub>2</sub>-CO<sub>2</sub>-H<sub>2</sub>O. *Russ. Geol. Geophys.* **1997**, *2*, 587–598.
38. Bataleva, Y.V.; Kruk, A.N.; Novoselov, I.D.; Furman, O.V.; Palyanov, Y.N. Decarbonation reactions involving ankerite and dolomite under upper mantle P, T-parameters: Experimental modeling. *Minerals* **2020**, *10*, 715. [[CrossRef](#)]
39. Tao, R.; Fei, Y.; Zhang, L. Experimental determination of siderite stability at high pressure. *Am. Min.* **2013**, *98*, 1565–1572. [[CrossRef](#)]
40. Mukherjee, B.K.; Sachan, H.K. Carbonate-bearing UHPM rocks from the Tso-Morari Region, Ladakh, India: Petrological implications. *Int. Geol. Rev.* **2003**, *45*, 49–69. [[CrossRef](#)]
41. Omori, S.; Liou, J.G.; Zhang, R.Y.; Ogasawara, Y. Petrogenesis of impure dolomitic marble from the Dabie mountains, central China. *Isl. Arc* **1998**, *7*, 98–114. [[CrossRef](#)]
42. Zhang, L.; Ellis, D.J.; Arculus, R.J.; Jiang, W.; Wei, C. ‘Forbidden zone’ subduction of sediments to 150 km depth—the reaction of dolomite to magnesite + aragonite in the UHPM metapelites from western Tianshan, China. *J. Metamorph. Geol.* **2003**, *21*, 523–529. [[CrossRef](#)]
43. Plank, T.; Manning, C.E. Subducting carbon. *Nature* **2019**, *574*, 343–352. [[CrossRef](#)] [[PubMed](#)]
44. Brey, G.P.; Bulatov, V.K.; Gurnis, A.V. Melting of K-rich carbonated peridotite at 6–10 GPa and the stability of K-phases in the upper mantle. *Chem. Geol.* **2011**, *281*, 333–342. [[CrossRef](#)]
45. Shatskiy, A.; Bekhtenova, A.; Podborodnikov, I.V.; Arefiev, A.V.; Litasov, K.D. Metasomatic interaction of the eutectic Na- and K-bearing carbonate melts with natural garnet lherzolite at 6 GPa and 1100–1200 °C: Toward carbonatite melt composition in SCLM. *Lithos* **2020**, *374*, 105725. [[CrossRef](#)]
46. Takahashi, E. Melting of a dry peridotite KLB-1 up to 14 GPa: Implications on the origin of peridotitic upper mantle. *J. Geophys. Res. Solid Earth* **1986**, *91*, 9367–9382. [[CrossRef](#)]
47. Hart, S.R.; Zindler, A. In search of a bulk-earth composition. *Chem. Geol.* **1986**, *57*, 247–267. [[CrossRef](#)]
48. Sokol, A.G.; Pal’yanov, Y.N.; Pal’yanova, G.A.; Tomilenko, A.A. Diamond crystallization in fluid and carbonate-fluid systems under mantle PT conditions: 1. Fluid composition. *Geochem. Intern.* **2004**, *42*, 830–838.
49. Palyanov, Y.N.; Kupriyanov, I.N.; Khokhryakov, A.F.; Borzdov, Y.M. High-pressure crystallization and properties of diamond from magnesium-based catalysts. *CrystEngComm.* **2017**, *19*, 4459–4475. [[CrossRef](#)]
50. Sokol, A.G.; Borzdov, Y.M.; Palyanov, Y.N.; Khokhryakov, A.F. High temperature calibration a multi-anvil high-pressure apparatus. *High Press. Res.* **2015**, *35*, 139–147. [[CrossRef](#)]
51. Aulbach, S.; Griffin, W.L.; Pearson, N.J.; O’Reilly, S.Y. Nature and timing of metasomatism in the stratified mantle lithosphere beneath the central Slave craton (Canada). *Chem. Geol.* **2013**, *352*, 153–169. [[CrossRef](#)]
52. Brooker, R.A.; Kohn, S.C.; Holloway, J.R.; McMillan, P.F.; Carroll, M.R. Solubility, speciation and dissolution mechanisms for CO<sub>2</sub> in melts on the NaAlO<sub>2</sub>-2 join. *Geochim. Cosmochim. Acta* **1999**, *63*, 3549–3565. [[CrossRef](#)]
53. Mysen, B. Structure–property relationships of COHN-saturated silicate melt coexisting with COHN fluid: A review of in-situ, high-temperature, high-pressure experiments. *Chem. Geol.* **2013**, *346*, 113–124. [[CrossRef](#)]
54. Eggler, D.H. The effect of CO<sub>2</sub> upon partial melting of peridotite in the system Na<sub>2</sub>O–CaO–Al<sub>2</sub>O<sub>3</sub>–MgO–SiO<sub>2</sub>–CO<sub>2</sub> to 35 kb, with an analysis of melting in a peridotite–H<sub>2</sub>O–CO<sub>2</sub> system. *Am. J. Sci.* **1978**, *278*, 305–343. [[CrossRef](#)]
55. Morizet, Y.; Vuilleumier, R.; Paris, M. A NMR and molecular dynamics study of CO<sub>2</sub>-bearing basaltic melts and glasses. *Chem. Geol.* **2015**, *418*, 89–103. [[CrossRef](#)]
56. Korschak, A.; Keppler, H. The speciation of carbon dioxide in silicate melts. *Contrib. Mineral. Petrol.* **2014**, *167*, 998. [[CrossRef](#)]
57. Yaxley, G.M.; Berry, A.J.; Kamenetsky, V.S.; Woodland, A.B.; Golovin, A.V. An oxygen fugacity profile through the Siberian Craton–Fe K-edge XANES determinations of Fe<sup>3+</sup>/ΣFe in garnets in peridotite xenoliths from the Udachnaya East kimberlite. *Lithos* **2012**, *140*, 142–151. [[CrossRef](#)]

58. Goncharov, A.G.; Ionov, D.A.; Doucet, L.S.; Pokhilenko, L.N. Thermal state, oxygen fugacity and C–O–H fluid speciation in cratonic lithospheric mantle: New data on peri-dotite xenoliths from the Udachnaya kimberlite, Siberia. *Earth Planet. Sci. Lett.* **2012**, *357*, 99–110. [[CrossRef](#)]
59. Stagno, V.; Ojwang, D.O.; McCammon, C.A.; Frost, D.J. The oxidation state of the mantle and the extraction of carbon from Earth's interior. *Nature* **2013**, *493*, 84–88. [[CrossRef](#)]
60. Tappe, S.; Foley, S.F.; Kjarsgaard, B.A.; Romer, R.L.; Heaman, L.M.; Stracke, A.; Jenner, G.A. Between carbonatite and lamproite—diamondiferous Torngat ultramafic lamprophyres formed by carbonate-fluxed melting of cratonic MARID-type metasomes. *Geochim. Cosmochim. Acta* **2008**, *72*, 3258–3286. [[CrossRef](#)]
61. Tappe, S.; Romer, R.L.; Stracke, A.; Steenfelt, A.; Smart, K.A.; Muehlenbachs, K.; Torsvik, T.H. Sources and mobility of carbonate melts beneath cratons, with implications for deep carbon cycling, metasomatism and rift initiation. *Earth Planet. Sci. Lett.* **2017**, *466*, 152–167. [[CrossRef](#)]
62. Creighton, S.; Stachel, T.; Matveev, S.; Hofer, H.; McCammon, C.; Luth, R.W. Oxidation of the Kaapvaal lithospheric mantle driven by metasomatism. *Contrib. Mineral. Petrol.* **2009**, *157*, 491–504. [[CrossRef](#)]
63. Palyanov, Y.N.; Shatsky, V.S.; Sobolev, N.V.; Sokol, A.G. The role of mantle ultrapotassic fluids in diamond formation. *Proc. Nat. Acad. Sci. USA* **2007**, *104*, 9122–9127. [[CrossRef](#)] [[PubMed](#)]
64. Palyanov, Y.N.; Sokol, A.G. The effect of composition of mantle fluids/melts on diamond formation processes. *Lithos* **2009**, *112*, 690–700. [[CrossRef](#)]
65. Palyanov, Y.N.; Sokol, A.G.; Khokhryakov, A.F.; Kruk, A.N. Conditions of diamond crystallization in kimberlite melt: Experimental data. *Rus. Geol. Geophys.* **2015**, *56*, 196–210. [[CrossRef](#)]
66. Wyllie, P.J.; Huang, W.L.; Otto, J.; Byrnes, A.P. Carbonation of peridotites and decarbonation of siliceous dolomites represented in the system CaO–MgO–SiO<sub>2</sub>–CO<sub>2</sub> to 30 kbar. *Tectonophysics* **1983**, *100*, 359–388. [[CrossRef](#)]
67. Stone, R.S.; Luth, R.W. Orthopyroxene survival in deep carbonatite melts: Implications for kimberlites. *Contrib. Mineral. Petrol.* **2016**, *171*, 63. [[CrossRef](#)]
68. Zhang, G.L.; Chen, L.H.; Jackson, M.G.; Hofmann, A.W. Evolution of carbonated melt to alkali basalt in the South China Sea. *Nat. Geosci.* **2017**, *10*, 229–235. [[CrossRef](#)]
69. Luth, R.W. The activity of silica in kimberlites, revisited. *Contrib. Mineral. Petrol.* **2009**, *158*, 283–294. [[CrossRef](#)]
70. Kamenetsky, V.S.; Yaxley, G.M. Carbonate–silicate liquid immiscibility in the mantle propels kimberlite magma ascent. *Geochim. Cosmochim. Acta* **2015**, *158*, 48–56. [[CrossRef](#)]
71. Pearson, D.G.; Canil, D.; Shirey, S.B. Mantle samples included in volcanic rocks: Xenoliths and diamonds. *Treatise Geochem. Ed.* **2014**, *2*, 170–253.
72. Liu, Z.; Ionov, D.A.; Nimis, P.; Xu, Y.; He, P.; Golovin, A.V. Thermal and compositional anomalies in a detailed xenolith-based lithospheric mantle profile of the Siberian craton and the origin of seismic midlithosphere discontinuities. *Geology* **2022**, *49*, 947. [[CrossRef](#)]